An Inversion of NO$_X$ and NMVOC Emissions using Satellite Observations during the KORUS-AQ Campaign and Implications for Surface Ozone over East Asia

Amir H. Souri[1*], Caroline R. Nowlan[1], Gonzalo González Abad[1], Lei Zhu[1,2], Donald R. Blake[3], Alan Fried[4], Andrew J. Weinheimer[5], Jung-Hun Woo[6], Qiang Zhang[7], Christopher E. Chan Miller[1], Xiong Liu[1], and Kelly Chance[1]

[1]Harvard-Smithsonian Center for Astrophysics, Cambridge, MA, USA
[2]School of Environmental Science and Engineering, Southern University of Science and Technology, Shenzhen, China
[3]Department of Chemistry, University of California, Irvine, Irvine, CA, USA
[4]Institute of Arctic & Alpine Research, University of Colorado, Boulder, CO, USA
[5]National Center for Atmospheric Research, Boulder, CO, USA
[6]Department of Advanced Technology Fusion, Konkuk University, Seoul, South Korea
[7]Department of Earth System Science, Tsinghua University, Beijing, China

* corresponding author: ahsouri@cfa.harvard.edu

Abstract. The absence of up-to-date emissions has been a major impediment to accurately simulate aspects of atmospheric chemistry, and to precisely quantify the impact of changes of emissions on air pollution. Hence, a non-linear joint analytical inversion (Gauss-Newton method) of both volatile organic compounds (VOC) and nitrogen oxides (NO$_x$) emissions is made by exploiting the Smithsonian Astrophysical Observatory (SAO) Ozone Mapping and Profiler Suite Nadir Mapper (OMPS-NM) formaldehyde (HCHO) and the National Aeronautics and Space Administration (NASA) Ozone Monitoring Instrument (OMI) tropospheric nitrogen dioxide (NO$_2$) retrievals during the Korea-United States Air Quality (KORUS-AQ) campaign over East Asia in May-June 2016. Effects of the chemical feedback of NO$_x$ and VOCs on both NO$_2$ and HCHO are implicitly included through iteratively optimizing the inversion. Emission uncertainties are greatly narrowed (averaging kernels>0.8, which is the mathematical presentation of the partition of information gained from the satellite observations with respect to the prior knowledge) over medium- to high-emitting areas such as cities and dense vegetation. The prior amount of total NO$_x$ emissions is mainly dictated by values reported in the MIX-Asia 2010 inventory. After the inversion we conclude a decline in the emissions (before, after, change) for China (87.94±44.09 Gg/day, 68.00±15.94 Gg/day, -23%), North China Plain (NCP) (27.96±13.49 Gg/day, 19.05±2.50

Gg/day, -32%), Pearl River Delta (PRD) (4.23±1.78 Gg/day, 2.70±0.32 Gg/day, -36%), Yangtze River Delta (YRD) (9.84±4.68 Gg/day, 5.77±0.51 Gg/day, -41%), Taiwan (1.26±0.57 Gg/day, 0.97±0.33 Gg/day, -23%), and Malaysia (2.89±2.77 Gg/day, 2.25±1.34 Gg/day, -22%), all of which have effectively implemented various stringent regulations. In contrast, South Korea (2.71±1.34 Gg/day, 2.95±0.58 Gg/day, +9%) and Japan (3.53±1.71 Gg/day, 3.96±1.04 Gg/day, +12%) experience an increase in NO_x emissions potentially due to risen number of diesel vehicles and new thermal power plants. We revisit the well-documented positive bias (by a factor of 2 to 3) of the MEGAN v2.1 in terms of biogenic VOC emissions in the tropics. The inversion, however, suggests a larger growth of VOC (mainly anthropogenic) over NCP (25%) than previously reported (6%) relative to 2010. The spatial variation in both magnitude and sign of NO_x and VOC emissions results in non-linear responses of ozone production/loss. Due to simultaneous decrease/increase of NO_x/VOC over NCP and YRD, we observe a ~53% reduction in the ratio of the chemical loss of NO_x (LNO_x) to the chemical loss of RO_x (RO_2+HO_2) transitioning toward NO_x-sensitive regimes, which in turn, reduces/increases the afternoon chemical loss/production of ozone through NO_2+OH (-0.42 ppbv hr^{-1})/HO_2 (and RO_2)+NO (+0.31 ppbv hr^{-1}). Conversely, a combined decrease in NO_x and VOC emissions in Taiwan, Malaysia, and southern China suppresses the formation of ozone. Simulations using the updated emissions indicate increases in maximum daily 8-hour average (MDA8) surface ozone over China (0.62 ppbv), NCP (4.56 ppbv), and YRD (5.25 ppbv), suggesting that emission control strategies on VOCs should be prioritized to curb ozone production rates in these regions. Taiwan, Malaysia, and PRD stand out as the regions undergoing lower MDA8 ozone levels resulting from the NO_x reductions occurring predominantly in NO_x-sensitive regimes.

Introduction

The study of ozone (O_3) formation within the troposphere in East Asia is of global importance. This significant pollutant is not confined to the source, as it spreads hemispherically through the air, affecting background concentrations as far away as the U.S. A study by Lin et al. [2017] provided modeling evidence of enhancements of springtime surface ozone levels (+0.5 ppbv yr^{-1}) in the western U.S. in 1980-2014 solely due to the tripling of Asian anthropogenic emissions over the period. As more studies have informed the impact of ozone pollution on both human health and crop yields, Chinese governmental regulatory agencies have begun to take action on cutting the amount of NO_x ($NO+NO_2$) emissions since 2011-2012 [Gu et al., 2013; Reuter et al., 2014; Krotkov et al., 2016; de Foy et al., 2016; Souri et al., 2017a]; however no effective policy on volatile organic compound (VOC) emissions had been put into effect prior to 2016 [Stavrakou et al., 2017; Souri et al., 2017a; Shen et al., 2019; Li et al., 2019], with an exception to Pearl River Delta (PRD) [Zhong et al. 2013]. In addition to China, a number of governments including those of Malaysia and Taiwan have put a great deal of effort into shifting their energy pattern from consuming fossil fuels to renewable sources [Trappey el al., 2012; Chua and Oh, 2011]. On the other hand, using satellite observations, Irie et al. [2016] and Souri et al. [2017a] revealed a systematic hiatus in the reduction of NO_x over South Korea and Japan potentially due to increases in the number of diesel vehicles and new thermal power plants built to compensate for the collapse of the Fukushima nuclear power plant in 2011. Therefore, it is interesting to quantify to what extent these policies have impacted ozone pollution.

Unraveling the origin of ozone is complicated by a number of factors encompassing the nonlinearity of ozone formation to its sources, primarily from NO_x and VOCs. Therefore, to be able to quantify the impact of recent emission changes, we have developed a top-down estimate of relevant emission inventories using well-characterized satellite observations. There are a myriad of studies focusing on optimizing the bottom-up anthropogenic and biogenic emissions using satellites observations, which provide high spatial coverage, in conjunction with chemical transport models for VOCs [e.g., Palmer et al., 2003; Shim et al., 2005; Curci et al., 2010; Stavrakou et al., 2009, 2011], and NO_x [e.g., Martin et al., 2003; Chai et al., 2009; Miyazaki et al., 2017; Souri et al., 2016a, 2017a, 2018]. Most inverse modeling studies do not consider both NO_2 and formaldehyde (HCHO) satellite-based observations to perform a joint-inversion. It has been shown that VOC and NO_x emissions can affect the production/loss of each other [Marais et al.,

2012; Wolfe et al. 2016; Valin et al., 2016; Souri et al., 2020]. Consequently, a joint method that incorporates both species while minimizing the uncertainties in their emissions is better suited to address this problem. Dealing with this tangled relationship between VOC-NO_2 and NO_x-HCHO requires an iteratively non-linear inversion framework able to incrementally consider the relationships derived from a chemical transport model. Here we will provide an optimal estimate of NO_x and VOC emissions during the KORUS-AQ campaign using the Smithsonian Astrophysical Observatory (SAO) Ozone Mapping and Profiler Suite Nadir Mapper (OMPS-NM) HCHO and the National Aeronautics and Space Administration (NASA) Ozone Monitoring Instrument (OMI) NO_2 retrievals whose accuracy and precisions are characterized against rich observations collected during the campaign. Having a top-down constraint on both emissions permits a more precise quantification of the impact of the recent emission changes on different chemical pathways pertaining to ozone formation and loss.

Measurements, Modeling and Method

Remote sensing measurements

OMPS HCHO

OMPS-NM onboard the Suomi National Polar-orbiting Partnership (Suomi NPP) is a UV-backscattered radiation spectrometer launched in October 2011 [Flynn et al., 2014]. Its revisit time is the same as other NASA A-Train satellites, including Aura at approximately 13:30 local time at the equator in ascending mode. OMPS-NM covers 300-380 nm with a resolution of 1 nm full-width half maximum (FWHM). The sensor has a 340×740 pixel charge-coupled device (CCD) array measuring the UV spectra at a spatial resolution of 50×50 km^2 at nadir. The HCHO retrieval has been fully described in González Abad et al. [2015; 2016]. Briefly, OMPS HCHO slant columns are fit using direct radiance fitting [Chance, 1998] in the spectral range 327.7-356.5 nm. The spectral fit requires a reference spectrum as function of the cross-track position as it attempts to determine the number of molecules with respect to a reference (i.e., a differential spectrum fitting). To account for this, we use earthshine radiances over a relatively pristine area in the remote Pacific Ocean within -30º to +30º latitudes. An upgrade to this reference correction is the use of daily HCHO profiles over monthly-mean climatological ones from simulations done by the GEOS-Chem chemical transport model. On average, this leads to a 4% difference in HCHO total columns with respect to using the monthly-mean climatological values (Figure S1). The scattering weights describing the sensitivity of the light path through a simulated atmosphere are calculated using

VLIDORT [Spurr, 2006]. The shape factors used for calculating air mass factors (AMFs) are derived from a regional chemical transport model (discussed later) that is used for carrying out the inversion in the present study. We remove unqualified pixels based on cloud fraction < 40%, solar zenith angle < 65°, and a main quality flag provided in the data. We oversample the HCHO columns for the period of May-June 2016 using a Cressman spatial interpolator with a 1° radius of influence.

OMI Tropospheric NO$_2$

We use NASA OMI tropospheric NO$_2$ (version 3.1) level 2 data whose retrieval is made in the violet/blue (402-465 nm) due to strong absorption of the molecule in this wavelength range [Levelt et al., 2018]. The sensor has a nadir spatial resolution of 13×24 km^2 which can extend to 40×160 km^2 at the edge of scanlines. A more comprehensive description of the retrieval and the uncertainty associated with the data can be found in Krotkov et al. [2017] and Choi et al. [2019]. We remove bad pixels based on cloud fraction < 20%, solar zenith angle < 65°, without the row anomaly, vertical column density (VCD) quality flag = 0, and Terrain Reflectivity < 30%. Similar to the OMPS HCHO, we recalculate AMFs by using shape factors from the chemical transport model used in this study. We oversample the OMI granules using the Cressman interpolator with a 0.25° radius of influence.

Model simulation

To be able to simulate the atmospheric composition, and to perform analytical inverse modeling, we set up a 27-km grid resolution regional chemical transport model using the Community Multiscale Air Quality Modeling System (CMAQ) model (v5.2.1, doi:10.5281/zenodo.1212601) [Byun and Schere, 2006] that consists of 328×323 grids covering China, Japan, South Korea, Taiwan and some portions of Russia, India and South Asia (Figure 1). The time period covered by the simulation is from April to June 2016. We use the month of April for spin-up. The anthropogenic emissions are based on the monthly MIX-Asia 2010 inventory [Li et al., 2015] in the CB05 mechanism. The anthropogenic emissions are mainly grouped into three different sectors, namely mobile, point, and residential (area) sources. We apply a diurnal scale to the mobile sectors used in the national emission inventory (NEI)-2011 emission platform to represent the first-order approximation of traffic patterns. We include biomass burning emissions from the Fire Inventory from NCAR (FINN) v1.6 inventory [Wiedinmyer et al., 2011], and consider the plume rise parametrization used in the GEOS-Chem model (i.e., 60% of emissions

are distributed uniformly in the planetary boundary layer (PBL)). We use the offline Model of Emissions of Gases and Aerosols from Nature (MEGAN) v2.1 model [Guenther et al., 2012] following the high resolution inputs described in Souri et al. [2017]. The diurnally-varying lateral chemical conditions are simulated by GEOS-Chem v10 [Bey et al., 2001] using the full chemistry mechanism (NO_x-O_x-HC-Aer-Br) spun up for a year. With regard to weather modeling, we use the Weather Research and Forecasting model (WRF) v3.9.1 [Skamarock et al., 2008] at the same resolution to that of the CMAQ (~27 km), but with a wider grid (342×337), and 28 vertical pressure sigma levels. The lateral boundary conditions and the grid nudging inputs are from the global Final (FNL) 0.25º resolution model. The major configurations for the WRF-CMAQ model are summarized in Table 1 and Table 2.

Inverse modeling

We attempt to improve our high-dimensional imperfect numerical representation of atmospheric compounds using the well-characterized NO_2 and HCHO columns from satellites. We use an analytical inversion using the WRF-CMAQ model to constrain the relevant bottom-up emission estimation [Souri et al., 2016; Souri et al., 2017a; Souri et al., 2018]. The inversion seeks to solve the following cost function under the assumptions that i) both observation and emission error covariances follow Gaussian probability density functions with a zero bias, ii) the observation and emission error covariances are independent and iii) the relationship between observations and emissions is not grossly non-linear:

$$J(\mathbf{x}) = \frac{1}{2}(\mathbf{y} - F(\mathbf{x}))^T \mathbf{S}_o^{-1}(\mathbf{y} - F(\mathbf{x})) + \frac{1}{2}(\mathbf{x} - \mathbf{x}_a)^T \mathbf{S}_e^{-1}(\mathbf{x} - \mathbf{x}_a) \tag{1}$$

where x is the inversion estimate (a posteriori) given two sources of data: a priori (x_a) and observation (y). $\mathbf{S}_o$ and $\mathbf{S}_e$ are the error covariance matrices of observation (instrument) and emission. F is the forward model (here WRF-CMAQ) to project the emissions onto columns. The first term of Eq.1 attempts to reduce the distance between observations and the simulated columns. The second term incorporates some prior understanding and expectation of the true state of the emissions. The weight of each term is dictated by its covariance matrix. If $\mathbf{S}_e$ is large compared to $\mathbf{S}_o$, the a posteriori will be independent of the prior knowledge and, conversely, if $\mathbf{S}_o$ dominates, the final solution will consist mostly of the a priori.

Following the Gauss-Newton method described in Rodger [2000], we derive iteratively (i.e., i is the index of iteration) the posterior emissions by:

$$\mathbf{x}_{i+1} = \mathbf{x}_a + \mathbf{G}[\mathbf{y} - F(\mathbf{x}_i) - K_i(\mathbf{x}_i - \mathbf{x}_a)] \tag{2}$$

where $\mathbf{G}$ is the Kalman gain,

$$\mathbf{G} = \mathbf{S}_e \, K_i^T \big(K_i \mathbf{S}_e \, K_i^T + \mathbf{S}_o \big)^{-1} \tag{3}$$

and $K_i \, (= K(\mathbf{x_i}))$ is the Jacobian matrix calculated explicitly from the model (discussed later). The covariance matrix of the a posteriori is calculated by:

$$\hat{\mathbf{S}}_e = (\mathbf{I} - \mathbf{G}\hat{K}^T)\mathbf{S}_e \tag{4}$$

where $\hat{K}$ is the Jacobian from the i*th* iteration. Here we iterate Eq.2 three times. The averaging kernels (**A**) are given by:

$$\mathbf{A} = \mathbf{I} - \hat{\mathbf{S}}_e \mathbf{S}_e^{-1} \tag{5}$$

The inversion system is complicated by the commonly overlooked fact that observations are biased. For instance, Souri et al. [2018] found that airborne remote sensing observations were high relative to surface Pandora measurements. The overestimation of the VCDs was problematic, since it could have been propagated in the inversion, inducing a bias in the top-down estimation. The authors partly mitigated it by constraining the MODIS albedo which was assumed to be responsible for the bias. Attempts to reduce the bias resulting from coarse profiles from a global model in calculating gas shape profiles were made by recalculating the shape factors using those from higher spatial resolution regional models in other studies [e.g., Souri et al., 2017; Laughner et al., 2018]. For this study, we use abundant observations from the KORUS-AQ campaign and follow the intercomparison platform proposed by Zhu et al. [2016; 2020] using aircraft observations collected during the campaign to be able to mitigate the biases in HCHO columns. Based on the corrected global model as a benchmark (Figure S2), we scale up all OMPS HCHO columns by 20%. To mitigate the potential biases in OMI NO_2, we followed exclusively the values reported over the KORUS-AQ period in Choi et al. [2019]. We increase the NO_2 concentration uniformly by 33.9% (see table A3 in the paper).

We calculate the covariance matrix of observations using the column uncertainty variable provided in the satellite datasets and consider them as random errors associated with spectrum fitting. We consider 25% random errors for the air mass factors. Therefore, these values (as random errors) are significantly lowered down by oversampling the data over the course of two months. In addition to that, we consider a fixed error for all pixels due to variability that exists in the applied bias correction (3.61×10^{15} molec.cm^{-2} for NO_2 and 4.62×10^{15} molec.cm^{-2} for HCHO). This error

is based on the RMSE obtained from the mentioned studies used for removing biases. Despite the fact that we do not account for non-diagonal elements of the covariance matrices, the incremental updates of **G** adjusted by both NO_2 and HCHO observations should better translate the covariance matrices into the emission space.

To increase the degree of freedom for the optimization, we combine all sector emissions including anthropogenic, biomass burning and biogenic emissions for NO_x and VOCs. Therefore, we use the following formula to estimate the variance of the a priori:

$$\sigma^2_{Total} = f^2_{Anthro} \times \sigma^2_{Anthro} + f^2_{BB} \times \sigma^2_{BB} + f^2_{Bio} \times \sigma^2_{Bio} \qquad (6)$$

where f denotes the fraction of the emission sector with respect to the total emissions, and σ is the standard deviation of each sector category which is calculated from the average of each sector to a relative error listed in Table 3.

For the same purpose (enhancing the amount of information gained from satellite observation) and to increase computational speed, we reduce the dimension of the state vectors (emissions) by aggregating them. However, grouping emissions into certain zones could also introduce another type of uncertainty, known as the aggregation error. We choose optimally aggregated zones by running the inversion multiple times, each with a certain selection of state vectors [Turner and Jacob, 2015]. As in our previous study in Souri et al. [2018], we use the Gaussian Model Mixture (GMM) method to cluster emissions into certain zones that share roughly similar features and investigate which combinations will lead to a minimum of the sum of aggregation and smoothing errors.

In order to create the K matrix, one must estimate the impact of changes in emissions for each of the aggregated zones to the concentrations of a target compound which is calculated using CMAQ-Direct Decoupled Method (DDM) [Dunker et al., 1989; Cohan et al., 2005]. For instance, the first row and column of K denoting the response of the first grid cell to a zonal emission can be obtained by:

$$K_{(1,1)} = \frac{S^{NO2}_{(1,1)}}{ENO_x^{Total,Zone}} \qquad (7)$$

where $S^{NO2}_{(1,1)}$ is the DDM output in units of molecule cm^{-2} for the first row and column. It explains the resultant change in NO_2 column by changing one unit of total NO_x emissions. We do not consider the interconnection between the zonal emissions and concentrations due to computational burdens; therefore, we assume that the HCHO and NO_2 columns are mostly confined to their

sources in the two-month averages. The same concept will be applied to HCHO and VOC emissions. The advantage of using CMAQ-DDM to estimate the sensitivity lies in the fact that it calculates the local gradient which better represents the non-linear relationship existing between the emissions and the columns [Souri et al., 2017a; Souri et al., 2018], which in turn, reduces the number of iterations.

Validation of the model in terms of meteorology

It is essential to first evaluate some key meteorological variables, because large errors in the weather can complicate the inversion [e.g., Liu et al. 2017]. In order to validate the performance of the WRF model in terms of a number of meteorological variables including surface temperature, relative humidity, and winds, we use more than 1100 surface measurements from integrated surface database (ISD) stations (https://www.ncdc.noaa.gov/isd) over the domain in May-June 2016. Table 4 lists the comparison of the model and the observations for the mentioned variables. Our model demonstrates a very low bias (0.6°C) with regard to surface temperature. We find a reasonable correspondence in terms of relative humidity indicating a fair water vapor budget in the model. The largest discrepancy between the model and observations in terms of temperature and humidity occurs in those grid cells that are in the proximity of the boundary conditions (not shown). Concerning the wind components, the deviation of the model from the observations is smaller than results obtained in a relatively flat area like Houston in Souri et al. [2016].

Comparison to satellites and providing top-down emissions

Prior to updating the emissions, we find it necessary to shed light on the spatial distribution of tropospheric NO_2 and HCHO total columns from both observations and model, and their potential differences relative to their key precursors' emissions. Subsequently, we report the results from the inverse modeling and the uncertainty associated with the top-down estimation; moreover, we wish to assess how much information is gained from utilizing satellite observations via the calculation of averaging kernels. Finally, observations are used to verify, to some extent, the accuracy of our top-down emission estimations.

NO_x

The first row in Figure 2 illustrates tropospheric NO_2 columns from the regional model, OMI (using adjusted AMF and bias corrected), and the logarithmic ratio of both quantities in May-June 2016 at ~1330 LST over Asia. The second row depicts daily-mean values of dominant sources of NO_x, namely as, biogenic, anthropogenic, and biomass burning emissions (that are subject to

change after the inversion). A high degree of correlation between the anthropogenic NO_x emissions and NO_2 columns implies the predominant production of NO_2 from the anthropogenic sources [Logan, 1983]. We find a reasonable two-dimensional Pearson correlation (r=0.73) between the modeled and the observed columns. Generally, the WRF-CMAQ largely underestimated (56%, -7.72×10^{14} molec.cm^{-2}) tropospheric NO_2 columns with respect to those of OMI over the entire domain. Segregating intuitively the domain into high emission areas (NO_x > 10 ton/day) and low ones (NO_x < 10 ton/day) allows for a better understanding of the discrepancy between the model and the observations. In the high NO_x areas, the model tends to overestimate tropospheric NO_2 columns by 73% (3.71×10^{15} molec.cm^{-2}), whereas for the low NO_x regions, the model shows a substantial underestimation by 68% (-8.97×10^{14} molec.cm^{-2}). Such a conflicting bias is confirmed by the contour map of the logarithm ratio of OMI to the model in Figure 2. The large overestimation of the model in terms of NO_2 over the polluted areas is explained by stringent regulations enacted in various countries in Asia; for instance, Chinese regulatory agencies have taken aggressive actions recently to cut anthropogenic NO_x emissions by implementing selective catalytic reduction in power plants, closing a number of coal power plants, and policies on transportation [Zhang et al., 2012; Liu et al., 2016; Reuter et al., 2015; de Foy et al., 2016; Krotkov et al., 2016; Souri et al., 2017a]. The highest positive bias in the model is observed over Shanxi Province in China, home to coal production, underscoring the effectiveness of the emission standards at controlling air pollution. Likewise, we observe a positive bias in the model over major cities in Japan and South Korea; but the magnitude of the reduction over these cities is substantially smaller than what we observe in China.

The underestimation of the model in the low NO_x regions is related to a number of factors such as i) the widely-reported underestimation of soil (biogenic) NO_x emissions due to the lack of precise knowledge of fertilizers use, soil biota, or canopy interactions [Jaeglé, et al., 2005; Hudman et al., 2010; Souri et al., 2016], ii) the underestimation of the upper-troposphere NO_2 due to non-surface emissions (aviation/lightning) or errors in the vertical mixing or moist convection [e.g., Souri et al., 2018], and iii) a possible overprediction of the lifetime of organic nitrates diminishing background NO_2 levels [Canty et al., 2015]. Addressing the second issue requires a very high resolution model with explicit resolving microphysics and large eddy simulations, and the last problem requires more experimental studies to improve organic nitrates chemistry [Romer Present et al., 2020]. In this study, we attempt to mitigate the discrepancy between the model and the

satellite observations solely by adjusting the relevant emissions. Accordingly, future improvements in physical/chemical processes of models will offset top-down emission estimates, inevitably.

The first row in Figure 3 shows the a priori, the a posteriori, and their ratios in terms of the total NO_x emissions in May-June 2016. We observe that the ratios are highly anti-correlated with those of OMI/CMAQ shown in Figure 2, suggesting that the inversion attempts to reduce the distance between the model and the observations. Major reductions occur over China. The enhancements in NO_x emissions are commonly found in rural areas, especially over grasslands located in the western/central China and Mongolia. The changes in NO_x emissions over South Korea and Japan are positive [Irie et al., 2016; Souri et al., 2017a] mainly due to rapid increases in the number of diesel cars in South Korea, and thermal power plants built as a substitution for the Fukushima nuclear plant in Japan. This is especially the case for Japan for which we observe a larger enhancement in total NO_x emissions (12%). The second row in Figure 3 depicts the relative errors in the a priori, the a posteriori, and AKs. Relative errors in the a priori are mostly confined to values close to 50% in polluted areas. They increase further, up to 100%, in areas experiencing relatively large contributions from biomass burning or biogenic (soil) emissions. Encouragingly, OMI tropospheric NO_2 columns in conjunction with the solid mathematical inversion method [Rodger, 2000] greatly reduce the uncertainties associated with the emissions in polluted areas; we observe AKs close to 1 over major cities or industrial areas. We see the lowest values in AKs over rural areas due to weaker signal/noise ratios from the sensor. Therefore, it is desirable but very difficult to improve the model using the sensor in terms of NO_x chemistry/emissions in remote areas, evident in the low values of AKs. Table 5 lists the magnitude of the total NO_x emissions in several regions (refer to Figure 1) before and after carrying out the inversion. If we assume that the dominant source of NO_x emissions is anthropogenic, the most successful countries at cutting emissions (before, after) are China (87.94±44.09 Gg/day, 68.00±15.94 Gg/day), Taiwan (1.26±0.57 Gg/day, 0.97±0.33 Gg/day), and Malaysia (2.89±2.77 Gg/day, 2.25±1.34 Gg/day). All three countries have successfully implemented plans to reduce anthropogenic emissions since 2010-2011 [Zhang et al., 2012; Trappey el al., 2012; Chua and Oh, 2011]. The uncertainty associated with the top-down estimate improves considerably. The largest reduction in the uncertainty of the emissions is observed over China, a response to a strong signal from OMI.

An interesting observation lies in the discrepancy between the logarithm-ratio of OMI/CMAQ (Figure 2) to that of the a posteriori to the a priori over the North China Plain (NCP), suggesting that using a bulk ratio [Martin et al., 2003] cannot fully account for possible chemical feedback. The logarithm-ratio of OMI/CMAQ is consistently lower than changes in the emission. Two reasons contribute to this effect: i) as NO_x emissions decrease in NO_x-saturated areas (i.e., the dominant sink of radicals is through NO_2+OH), OH levels essentially increase resulting in a shorter lifetime in NO_2; therefore to reduce NO_2 concentrations, a substantial reduction in NO_x (suggested by OMI/CMAQ) is unnecessary coinciding with results from the inverse modeling, ii) the CMAQ-DDM (Figure S3) suggests that NO_2 columns decrease due to increasing VOC emissions over the region; accordingly, the cross-relationship between NO_2 concentrations and VOC emissions partly adds to the discrepancy. It is because of the chemical feedback that recent studies have attempted to enhance the capability of inverse modeling by iteratively adjusting relevant emissions [e.g., Cooper et al., 2017; Li et al., 2019]. Likewise, our iterative non-linear inversion shows a superior performance over traditional bulk ratio methods, in part because it considered incrementally the chemical feedback.

To assess the resulting changes in the tropospheric NO_2 columns after the inversion, and to validate our results, we compare the simulated values using the a priori and the a posteriori with OMI in Figure 4. We observe 64% reduction in the tropospheric NO_2 columns on average over NCP despite only 32% reduction in the total NO_x emissions over the region, a result of the chemical feedback. The two-dimensional Pearson correlation between the simulation using the a posteriori and OMI increases from 73% (using the a priori) to 83%. Both datasets now are in a better agreement as far as the magnitude goes. However, we do not see a significant change in the background values in the new simulation compared to those of OMI due to less certain column observations.

To further validate the results, we compare the NO_2 data from the NCAR's four-channel chemiluminescence instrument onboard the DC-8 aircraft during the campaign (Figure S4). These data are not interfered by NO_z family. The aircraft collected the data in the Korean Peninsula around 23 days in May-June 2016 covering various altitudes and hours (https://www-air.larc.nasa.gov/cgi-bin/ArcView/korusaq, access date: December 2019). We observe an underestimation of NO_2 at the near surface levels (<900 hPa) by 19% (DC8 = 4.50 ppbv, CMAQ

= 3.67 ppbv). The updated emissions increase the near surface levels over the Korean Peninsula, which in turn, reduce the bias to 11% (CMAQ = 4.02 ppbv).

360 ***VOC***

A comparison between HCHO columns from the model and OMPS along with the major sources of VOCs in May-June 2016 is depicted in Figure 5. Anthropogenic VOCs are emitted from various sources such as solvent use, mobile, and chemical industries [Liu et al., 2008a,b]. A reasonable correlation (r=0.78) between the model and OMPS suggests a good confidence in the

365 location of emissions. However, the magnitude of HCHO columns between the two datasets strongly disagrees, especially over the tropics where biogenic emissions are large. A myriad of studies have reported a largely positive bias (by a factor of 2-3) associated with isoprene emissions estimated by MEGAN using satellite measurements [e.g., Millet et al., 2008; Stavrakou et al., 2009; Marais et al., 2012; Bauwens et al., 2016]. To compound, Stavrakou et al. [2011] found a

370 large overestimation in methanol emissions from the same model that can further preclude the accurate estimation of the yield of HCHO. This is especially the case for the tropics. As a response to the overestimation of the biogenic VOCs by MEGAN, we observe a largely positive bias in the simulated HCHO columns ranging from 50% over the south of China to ~400% over Malaysia and Indonesia. As we move away from the hotspot of the biogenic emissions in lower latitudes,

375 the positive bias of the model declines, ultimately turning into a negative bias at higher latitudes. OMPS HCHO columns suggest that the concentration of HCHO over NCP and Yangtze River Delta (YRD) is comparable to those over the tropics suggesting that the anthropogenic emissions over NCP are the dominant source of HCHO [Souri et al., 2017a; Jin and Holloway, 2015]. We do not see a significant deviation in the model from the observations over this region indicating that

380 no noticeable efforts on controlling VOC emissions in NCP and YRD have been made which is very likely due to the fact that the recent regulations over China have overlooked cutting emissions from several industrial sectors [Liu et al., 2016] prior to 2016 [Li et al. 2019]. For instance, Stavrakou et al. [2017] reported ~6% increases in anthropogenic VOC emissions over China from 2010 to 2014. The underestimation of the model with respect to OMPS lines up with results

385 reported by Souri et al. [2017a] and Shen et al. [2019]. We observe both underestimated and overestimated values in the simulated HCHO columns over areas in South Korea and Japan. The underestimation of HCHO in the model over regions with low VOCs (such as Mongolia and

Pacific Ocean) can be either due to missing sources or the incapability of CMAQ to account for moist convective transport.

390   Figure 6 illustrates the total VOC emissions before and after the inversion along with their errors. Immediately apparent is the large reduction of VOC emissions in the tropics and subtropics due to the overestimation of isoprene from MEGAN v2.1. In contrast, enhancements of the emissions are evident at higher latitudes. We observe that the dominantly anthropogenic VOC emissions over NCP increase (~25%) after the adjustment. Despite the presence of vegetation over

395   Japan and South Korea, we do not see largely overestimated values in the emissions. Hence, the overestimation of isoprene emissions is more pronounced in the tropics possibly because of an overestimation in the emission factors used for specific plants. Nevertheless, a non-trivial oversight in models could be an insufficient representation of both HO_x chemistry and dry deposition in forest canopies [Millet et al., 2008]; as a result, the net amount of HCHO in the

400   atmosphere over forest areas is higher than what should be if removal through either a chemical loss or a faster dry deposition is considered.

        Owing to the fact that we assume anthropogenic VOC emissions to be less uncertain relative to other sectors, the errors in the a priori are smaller in populated areas. We observe that OMPS HCHO columns are able to significantly reduce the uncertainty associated with the total

405   VOC emissions over areas showing a strong HCHO signal ($>10^{16}$ molec.cm^{-2}). Over clean areas, it is the other way around; we see less confidence in our top-down estimate (AK<0.4) in areas such as Tibet and Mongolia.

        We then compare the simulated HCHO column using two different emission inventories with those of OMPS in Figure 7. We observe a substantial improvement both in the spatial

410   structure and the magnitude of simulated HCHO columns using the a posteriori with respect to OMPS. The two-dimensional Pearson correlation increases from 0.78 to 0.91 after applying the adjustments to the emissions. In response to the increases in the total VOC emissions over the NCP, we observe ~11% enhancements in the simulated HCHO total columns. The updated emissions lead to a reduction in HCHO total columns as large as 70% in the tropics.

415   Validation of the model in terms of VOCs is not a straightforward task because the chemical mechanism used for our model has lumped several VOC species such as terminal/internal olefin or paraffin, only a handful of which were measured during the campaign. Besides, the MIX-Asia inventory estimates the anthropogenic emissions for a selected number of VOCs in the CB05

mechanism. Here, we focus only on six compounds including isoprene, HCHO, ethene, ethane,

420   acetaldehyde, and methanol whose emissions are adjusted (with the same factor) based on satellite

measurements. The comparison of the simulated values with the DC-8 measurements showed a

noticeable mitigation in the discrepancy between two datasets at lower boundaries (<900 hPa) in

terms of isoprene (Figure S5), ethane (Figure S6), ethene (Figure S7), and acetaldehyde (Figure

S8). Surprisingly, we observe a large underestimation of methanol over the Korean Peninsula by

425   a factor of ten (Figure S9). The same tendency was observed in other regions in Wells et al. [2014]

(see Figure 8 in the paper). Our inversion obviously fails at mitigating the bias as there is not much

direct information from the satellite observations on this compound. Wells et al. [2014] and Hu et

al. [2011] demonstrated that methanol can be a secondary source of HCHO up to 10-20% in

midlatitudes in warm seasons. We tend to underestimate HCHO concentrations (by 15%) in the

430   lower atmosphere (<900 hPa) after using the a posteriori over the Korean Peninsula (Figure S10).

Implications for surface ozone

The results we have generated can be further exploited to elucidate changes in the ozone

production rates $P(O_3)$ due to having the constrained NO_x and VOC emissions. We calculate $P(O_3)$

by subtracting the ozone loss driven by HO_x ($HO+HO_2$), reaction with several VOCs (i.e., alkenes

435   and isoprene), the formation of HNO_3, and O_3 photolysis followed by the reaction of $O(^1D)$ with

water vapor, from the ozone formation via removal of NO through HO_2 or RO_2:

$$P(O_3) = k_{HO_2+NO}[HO_2][NO] + \sum k_{RO_{2i}+NO}[RO_{2i}][NO]$$
$$- k_{OH+NO_2+M}[OH][NO_2][M] - k_{HO_2+O_3}[HO_2][O_3] \qquad (8)$$
$$- k_{OH+O_3}[OH][O_3] - k_{O(^1D)+H_2O}[O(^1D)][H_2O] - L(O_3 + VOCs)$$

Since $P(O_3)$ is a non-linear function of NO_x and VOC emissions, it is advantageous to look at the

ratio of chemical loss of NO_x to that of RO_x (RO_2+HO_2), a robust indicator to pinpointing

underlying drivers for RO_x cycle. LRO_x is defined through the sum of primarily radical-radical

440   reactions:

$$LRO_x = k_{HO_2+HO_2}[HO_2]^2 + \sum k_{RO_{2i}+HO_2}[RO_{2i}][HO_2] + \sum k_{RO_{2i}+RO_{2i}}[RO_{2i}]^2 \qquad (9)$$

LNO_x mainly occurs via the NO_2+OH reaction:

$$LNO_x = k_{OH+NO_2+M}[OH][NO_2][M] \qquad (10)$$

Typically, a value of $LNO_x/LRO_x{\sim}2.7$ defines the transition line between VOC-sensitive and

NO_x-sensitive regimes [Schroeder et al., 2017; Souri et al., 2020].

Figure 8 depicts a contour map of LNO_x/RO_x ratios before and after the inversion. As expected, the larger ratios are confined within major cities or industrial areas due to abundant NO_x emissions. The hotspot of VOC-sensitive regimes is located in NCP and YRD. Also of interest in Figure 8 is that advection renders a major fraction of the Yellow Sea (the sea connecting China to Korea) VOC-sensitive. Using the a posteriori leads to precipitous changes in the chemical regimes. As a result of a large reduction in the isoprene emissions in both the tropics and subtropics, we observe a shift toward VOC-limited, though the values of LNO_x/RO_x are yet too far from the transition line (i.e., $\ll 2.7$). The substantial reduction in NO_x emissions and an increase in VOC emissions over NCP and YRD go hand-in-hand transitioning towards NO_x-sensitive regime. The ratios over South Korea and Japan are found to be variable and somehow in synch with the changes in NO_x emissions.

The resultant changes in the LNO_x/LRO_x ratios shed some light on ozone sensitivity with respect to its major precursors, but $P(O_3)$ is also dependent on the absolute values of emissions, the degree of reactivity of VOCs, and the abundance of radicals. Here we use the integrated reaction rates (IRR) to determine the most influential reactions pertaining to ozone loss and production at the surface. We focus on 1200 to 1800 China standard time (CST) hours. Figure 9 shows the differences in the major pathways for the loss and the formation of ozone at the surface within the time window. The differences are computed based on the subtraction of the simulation with the a posteriori from that with the a priori. In Figure 9 we see a strong degree of correlation between the changes in magnitude of $P(O_3)$ through HO_2+NO reaction with those of NO_x emissions (Figure 3), whereas the changes in magnitude of $P(O_3)$ via RO_2+NO reaction primarily are on par with those of VOC emissions (Figure 6). We observe $P(O_3)$ increases through HO_2+NO and RO_2+NO reactions in Japan, South Korea, Myanmar, and Philippines because of increases in NO_x emissions in NO_x-sensitive regions. The simultaneous decrease in NO_x and VOC in PRD and Taiwan causes the production of ozone via the same pathways to reduce.

Normally, in VOC-rich environments, reduction in VOC emissions boosts OH concentrations (Figure S11). Consequently, we observe an enhancement of NO_2+OH reaction in the tropics and subtopics. A substantial reduction in the chemical loss of ozone through NO_2+OH over NCP and YRD arises from a considerable decrease of NO_x emissions and an increase in OH (due to chemical feedback of NO_x). In response to increase in HO_x concentrations over NCP (Figure S11-S12), we observe an enhancement of ozone loss through O_3+HO_x. The ozone

photolysis (O^1D+H_2O) are majorly driven by photolysis and water vapor mixing ratios, both of which are roughly constant in both simulations; accordingly the difference map of O^1D+H_2O is mainly reflecting changes in ozone concentrations (shown later). Interestingly, we observe a large reduction in the loss of ozone through reaction with VOCs at lower latitudes. This is essentially because of the reduction in $ISOP+O_3$, a VOC that prevails in those latitudes. Despite a much slower reaction rate for $ISOP+O_3$ compared to $ISOP+OH$ and $ISOP+h\nu$ [Karl et al. 2004], this specific chemical pathway can be important as a way to oxidize isoprene and form HO_x in forests [Paulson and Orlando, 1996].

Figure 10 sums the differences of all mentioned chemical pathways involved in formation/loss of surface ozone at 1200-1600 CST. Because of a complex non-linear relationship between $P(O_3)$ and its precursors, we observe a variability in both the sign and amplitude of $P(O_3)$. On average, changes in O_3 production dominate over changes in O_3 sinks except in Malaysia which underwent a significant reduction in isoprene emissions, thus slowing down the $ISOP+O_3$ reaction. In general, the differences in $P(O_3)$ follow the changes in the NO_x emissions depending on which chemical regimes prevail.

Much of the above analysis is based on ozone production rates, however, various parameters encompassing dry deposition, vertical diffusion, and advection can also affect ozone concentrations. Therefore we further compute the difference between the simulated maximum daily 8-h average (MDA8) surface ozone levels before and after the inversion depicted in Figure 11. For comparison, we also overplot the Chinese air quality monitoring network observations (https://quotsoft.net/air/) to have a general grasp of the performance of the model before and after adjusting the emissions. We see a striking correlation between $P(O_3)$ (right panel in Figure 10) and MDA8 surface ozone indicating that the selected chemical pathways in this study can explain ozone changes. Nonetheless, the transport obviously plays a vital role in the spatial variability associated with the differences of surface ozone [e.g., Souri et al., 2016b]. Figure 11 suggests a significant enhancement of ozone over NCP (~4.56 ppbv, +5.6%) and YRD (5.2 ppbv, +6.8%) due to simultaneous decreases/increases in NO_x/VOCs which is in agreement with Li et al. [2019]. On the other hand, reductions in NO_x mitigate ozone pollution in PRD (-5.4%), Malaysia (-5.6%) and Taiwan (-11.6%). Table 6 lists the simulated MDA8 surface ozone levels for several regions before and after updating the emissions. Increases in MDA8 ozone over NCP and YRD overshadow decreases in southern China resulting in 1.1% enhancement for China. This provides

strong evidence that regulations on cutting VOC emissions should not be ignored. The largest reduction/increase of MDA8 ozone is found over Taiwan/YRD. Comparisons with surface observations show that the model generally captured the ozone spatial distributions; however, it tends to largely overpredict MDA8 surface ozone (~ 7 ppbv). This tendency has been well-documented in other studies [e.g., Travis et al., 2016; Souri et al., 2017b; Lu et al., 2019]. The updated simulation with the top-down emission partly reduces this overestimation in southern regions of China, while it further exacerbates the overestimation in the northern parts. No doubt much of this stems from the fact that the preexisting biases associated with the model (beyond emissions such as vertical mixing and cloud optical thickness) mask any potential improvement expected from the constrained emissions. Because of this, in addition to adjusting relevant emissions, a direct assimilation of ozone concentrations should complementarily be exploited [e.g., Miyazaki et al., 2019] to bolster the capability of the model at simulating ozone.

Summary

In this paper we have focused on providing a top-down constraint on both volatile organic compound (VOC) and nitrogen oxides (NO_x) emissions using a combination of error-characterized Smithsonian Astrophysical Observatory (SAO) Ozone Mapping and Profile Suite Nadir Mapper (OMPS-NM) formaldehyde (HCHO) and National Aeronautics and Space Administration (NASA) Ozone Monitoring Instrument (OMI) nitrogen dioxide (NO_2) retrievals during the Korean and United States (KORUS) campaign over East Asia in May-June 2016. Here, we include biogenic, biomass burning and anthropogenic emissions from MEGAN, FINN, and MIX-Asia 2010 inventory, respectively. A key point is that by considering together the satellite observations, we have been able to not only implicitly take the chemical feedback existing between HCHO-NO_x and NO_2-VOC into account through iteratively optimizing an analytical non-linear inversion, but also to quantify the impact of recent changes in emissions (since 2010) on surface ozone pollution.

Concerning total NO_x emissions, the inversion estimate suggests a substantial reduction over China (-23%), North China Plain (NCP) (-32%), Pearl River Delta (PRD) (-36%), Yangtze River Delta (YRD) (-41%), Taiwan (-23%), and Malaysia (-22%) with respect to the values reported in the prior emissions mostly dictated by the MIX-Asia 2010 inventory. In essence these values reflect recent actions to lower emissions in those countries [Zhang et al., 2012; Trappey el al., 2012; Chua and Oh, 2011]. The analytical inversion also paves the way for estimating the averaging kernels (AKs), thereby informing the amount of information acquired from satellites on

the emissions estimation. We observe AKs>0.8 over major polluted areas indicating that OMI is able to improve the emission estimates over medium to high-emitting regions. Conversely, AKs are found to be small over pristine areas suggesting that little information can be gained from the satellite over rural areas given retrieval errors. In line with the studies of Irie et al. [2016] and Souri et al. [2017a], we observe a growth in the total NO_x emissions in Japan (12%) and South Korea (+9%) which are partially explained by new construction of thermal power plants in Japan, and an upward trend in the number of diesel vehicles in South Korea.

MEGAN v2.1 estimates too much isoprene emissions in the tropics and subtropics, a picture that emerges from the latitudinal dependence of the posterior VOC emissions to the prior ones. It is readily apparent from the top-down constrained VOC emissions that the prevailing anthropogenic VOC emissions in NCP is underestimated by 25%, a direction that is in agreement with studies by Souri et al. [2017] and Shen et al. [2019]. We find out that OMPS HCHO columns can greatly reduce the uncertainty associated with the total VOC emissions (AKs>0.8) over regions having a moderate-strong signal ($>10^{16}$ molec.cm^{-2}).

A large spatial variability associated with both NO_x and VOC results in great oscillation in chemical conditions regimes (i.e., NO_x-sensitive or VOC-sensitive). Due to considerable reduction/increase in NO_x/VOC emissions in NCP and YRD, we observe a large increase (53%) in the ratio of the chemical loss of NO_x (LNO_x) to the chemical loss of RO_x (RO_2+HO_2) shifting the regions towards NO_x-sensitive. As a result, a substantial reduction in afternoon NO_2+OH reaction rate (a major loss of O_3), and an increase in afternoon $NO+HO_2$ and RO_2+NO (a major production pathway for O_3) are observed, leading to enhancements of the simulated maximum daily 8-hr average (MDA8) surface ozone concentrations by ~5 ppbv. Therefore, additional regulations on VOC emissions should be implemented to battle ozone pollution in those areas. On the other hand, being predominantly in NO_x-sensitive regimes favors regions including Taiwan, Malaysia and PRD to benefit from reductions in NO_x, resulting in noticeable decreases in simulated MDA8 surface ozone levels. The comparison of simulated ozone before and after adjusting emissions and Chinese surface air quality observations reveal a large systematic positive bias (~ 7 ppbv) which hinders attaining the benefits from a more accurate ozone production rate due to the observationally-constrained NO_x/VOC ratios. This highlights the need to explicitly deal with other underlying issues in the model [e.g., Travis et al., 2016] to be able to properly simulate surface ozone.

It has taken many years to develop satellite-based gas retrievals, and weather and chemical transport models accurate enough to enable observationally-based estimates of emissions with reasonable confidence and quantified uncertainty, and produce credible top-down emission inventories over certain areas. However it is essential to improve certain aspects to be able to narrow the range of uncertainty associated with the estimation such as spatiotemporally varying bias of the satellite gas retrievals ii) the lack of precise knowledge of prior errors in the bottom-up emissions, iii) the model parameter errors including those from PBL, radiation, and winds should be propagated to the final output [e.g., Rodger 2000], iv) due to intertwined chemical feedback between various chemical compounds, inverse modeling needs to properly incorporate all available information (beyond HCHO and NO_2) considering the cross-relationship either explicitly or implicitly. Despite these limitations, this research demonstrated that a joint inversion of NO_x and VOC emissions using well-characterized observations significantly improved the simulation of HCHO and NO_2 columns, permitting an observationally-constrained quantification of the response of ozone production rates to the emission changes.

Acknowledgment

We are thankful for the funding from NASA Aura Science Team (#NNX17AH47G), NASA Science of Terra, Aqua and Suomi NPP (#80NSSC18K0691), NASA Making Earth System Data Records for Use in Research Environments (#80NSSC18M0091), and NOAA AC4 program (#NA18OAR4310108). We acknowledge the publicly available WRF, CMAQ, GEOS-Chem models, and KORUS-AQ data that make this study possible. The simulations were run on the Smithsonian Institution High Performance Cluster (SI/HPC) (https://doi.org/10.25572/SIHPC).

Data Availability

The top-down emission inventories estimated from this study can be found from: http://dx.doi.org/10.17632/8s4jscy93m.1

Authors' contributions

A.H.S designed the research, analyzed the data, conducted the inverse modeling, CMAQ, GEOS-Chem, WRF, and MEGAN, made all figures and wrote the manuscript. C.R.N, G.G, C.E.C.M, X.L. and K.C retrieved OMPS HCHO columns and conceived the study. L.Z. validated OMPS HCHO. D.R.B, A.F, and A.J.W measured different compounds during the campaign. J.W and Q.Z provided MIX-Asia inventory. All authors contributed to discussions and edited the manuscript.

References

Bauwens, M., Stavrakou, T., Müller, J.-F., Smedt, I.D., Roozendael, M.V., Werf, G.R. van der, Wiedinmyer, C., Kaiser, J.W., Sindelarova, K., Guenther, A., 2016. Nine years of global hydrocarbon emissions based on source inversion of OMI formaldehyde observations. Atmospheric Chemistry and Physics 16, 10133–10158. https://doi.org/10.5194/acp-16-10133-2016

Bey, I., Jacob, D.J., Yantosca, R.M., Logan, J.A., Field, B.D., Fiore, A.M., Li, Q., Liu, H.Y., Mickley, L.J., Schultz, M.G., 2001. Global modeling of tropospheric chemistry with assimilated meteorology: Model description and evaluation. Journal of Geophysical Research: Atmospheres 106, 23073–23095. https://doi.org/10.1029/2001JD000807

Byun, D., Schere, K.L., 2006. Review of the Governing Equations, Computational Algorithms, and Other Components of the Models-3 Community Multiscale Air Quality (CMAQ) Modeling System. Appl. Mech. Rev 59, 51–77. https://doi.org/10.1115/1.2128636

Canty, T.P., Hembeck, L., Vinciguerra, T.P., Anderson, D.C., Goldberg, D.L., Carpenter, S.F., Allen, D.J., Loughner, C.P., Salawitch, R.J., Dickerson, R.R., 2015. Ozone and NOx chemistry in the eastern US: evaluation of CMAQ/CB05 with satellite (OMI) data. Atmospheric Chemistry and Physics 15, 10965–10982. https://doi.org/10.5194/acp-15-10965-2015

Chai, T., Carmichael, G.R., Tang, Y., Sandu, A., Heckel, A., Richter, A., Burrows, J.P., 2009. Regional NOx emission inversion through a four-dimensional variational approach using SCIAMACHY tropospheric NO2 column observations. Atmospheric Environment 43, 5046–5055. https://doi.org/10.1016/j.atmosenv.2009.06.052

Chance, K., 1998. Analysis of BrO measurements from the Global Ozone Monitoring Experiment. Geophysical Research Letters 25, 3335–3338. https://doi.org/10.1029/98GL52359

Choi, S., Lamsal, L.N., Follette-Cook, M., Joiner, J., Krotkov, N.A., Swartz, W.H., Pickering, K.E., Loughner, C.P., Appel, W., Pfister, G., Saide, P.E., Cohen, R.C., Weinheimer, A.J., Herman, J.R., 2019. Assessment of NO2 observations during DISCOVER-AQ and KORUS-AQ field campaigns. Atmospheric Measurement Techniques Discussions 1–43. https://doi.org/10.5194/amt-2019-338

Chua, S.C., Oh, T.H., 2011. Green progress and prospect in Malaysia. Renewable and Sustainable Energy Reviews 15, 2850–2861. https://doi.org/10.1016/j.rser.2011.03.008

Cohan, D.S., Hakami, A., Hu, Y., Russell, A.G., 2005. Nonlinear Response of Ozone to Emissions: Source Apportionment and Sensitivity Analysis. Environ. Sci. Technol. 39, 6739–6748. https://doi.org/10.1021/es048664m

Cooper, M., Martin, R.V., Padmanabhan, A., Henze, D.K., 2017. Comparing mass balance and adjoint methods for inverse modeling of nitrogen dioxide columns for global nitrogen oxide emissions. Journal of Geophysical Research: Atmospheres 122, 4718–4734. https://doi.org/10.1002/2016JD025985

Curci, G., Palmer, P.I., Kurosu, T.P., Chance, K., Visconti, G., 2010. Estimating European volatile organic compound emissions using satellite observations of formaldehyde from the Ozone Monitoring Instrument. Atmospheric Chemistry and Physics 10, 11501–11517. https://doi.org/10.5194/acp-10-11501-2010

de Foy, B., Lu, Z., Streets, D.G., 2016. Satellite NO 2 retrievals suggest China has exceeded its NO x reduction goals from the twelfth Five-Year Plan. Scientific Reports 6, 1–9. https://doi.org/10.1038/srep35912

645   Dunker, A.M., 1984. The decoupled direct method for calculating sensitivity coefficients in chemical kinetics. J. Chem. Phys. 81, 2385–2393. https://doi.org/10.1063/1.447938

Flynn, L., Long, C., Wu, X., Evans, R., Beck, C.T., Petropavlovskikh, I., McConville, G., Yu, W., Zhang, Z., Niu, J., Beach, E., Hao, Y., Pan, C., Sen, B., Novicki, M., Zhou, S., Seftor, C., 2014. Performance of the Ozone Mapping and Profiler Suite (OMPS)
650   products. Journal of Geophysical Research: Atmospheres 119, 6181–6195. https://doi.org/10.1002/2013JD020467

González Abad, G., Liu, X., Chance, K., Wang, H., Kurosu, T.P., Suleiman, R., 2015. Updated Smithsonian Astrophysical Observatory Ozone Monitoring Instrument (SAO OMI) formaldehyde retrieval. Atmospheric Measurement Techniques 8, 19–32.
655   https://doi.org/10.5194/amt-8-19-2015

González Abad, G., Vasilkov, A., Seftor, C., Liu, X., Chance, K., 2016. Smithsonian Astrophysical Observatory Ozone Mapping and Profiler Suite (SAO OMPS) formaldehyde retrieval. Atmospheric Measurement Techniques 9, 2797–2812. https://doi.org/10.5194/amt-9-2797-2016
660   Gu, D., Wang, Y., Smeltzer, C., Liu, Z., 2013. Reduction in NOx Emission Trends over China: Regional and Seasonal Variations. Environ. Sci. Technol. 47, 12912–12919. https://doi.org/10.1021/es401727e

Guenther, A.B., Jiang, X., Heald, C.L., Sakulyanontvittaya, T., Duhl, T., Emmons, L.K., Wang, X., 2012. The Model of Emissions of Gases and Aerosols from Nature version 2.1
665   (MEGAN2.1): an extended and updated framework for modeling biogenic emissions. Geoscientific Model Development 5, 1471–1492. https://doi.org/10.5194/gmd-5-1471-2012

Hu, L., Millet, D.B., Mohr, M.J., Wells, K.C., Griffis, T.J., Helmig, D., 2011. Sources and seasonality of atmospheric methanol based on tall tower measurements in the US Upper
670   Midwest. Atmospheric Chemistry and Physics 11, 11145–11156. https://doi.org/10.5194/acp-11-11145-2011

Hudman, R.C., Russell, A.R., Valin, L.C., Cohen, R.C., 2010. Interannual variability in soil nitric oxide emissions over the United States as viewed from space. Atmospheric Chemistry and Physics 10, 9943–9952. https://doi.org/10.5194/acp-10-9943-2010
675   Irie, H., Muto, T., Itahashi, S., Kurokawa, J., Uno, I., 2016a. Turnaround of Tropospheric Nitrogen Dioxide Pollution Trends in China, Japan, and South Korea. Sola 12, 170–174. https://doi.org/10.2151/sola.2016-035

Jaeglé, L., Steinberger, L., Martin, R.V., Chance, K., 2005. Global partitioning of NOx sources using satellite observations: Relative roles of fossil fuel combustion, biomass burning and
680   soil emissions. Faraday Discuss. 130, 407–423. https://doi.org/10.1039/B502128F

Jin, X., Holloway, T., 2015. Spatial and temporal variability of ozone sensitivity over China observed from the Ozone Monitoring Instrument. Journal of Geophysical Research: Atmospheres 120, 7229–7246. https://doi.org/10.1002/2015JD023250

Karl, M., Brauers, T., Dorn, H.-P., Holland, F., Komenda, M., Poppe, D., Rohrer, F., Rupp, L.,
685   Schaub, A., Wahner, A., 2004. Kinetic Study of the OH-isoprene and O3-isoprene reaction in the atmosphere simulation chamber, SAPHIR. Geophysical Research Letters 31. https://doi.org/10.1029/2003GL019189

Krotkov, N.A., McLinden, C.A., Li, C., Lamsal, L.N., Celarier, E.A., Marchenko, S.V., Swartz, W.H., Bucsela, E.J., Joiner, J., Duncan, B.N., Boersma, K.F., Veefkind, J.P., Levelt, P.F.,
690   Fioletov, V.E., Dickerson, R.R., He, H., Lu, Z., Streets, D.G., 2016. Aura OMI

observations of regional SO2 and NO2 pollution changes from 2005 to 2015. Atmospheric Chemistry and Physics 16, 4605–4629. https://doi.org/10.5194/acp-16-4605-2016

Laughner, J.L., Zhu, Q., Cohen, R.C., 2018. The Berkeley High Resolution Tropospheric NO2 product. Earth System Science Data 10, 2069–2095. https://doi.org/10.5194/essd-10-2069-2018

Levelt, P.F., Joiner, J., Tamminen, J., Veefkind, J.P., Bhartia, P.K., Stein Zweers, D.C., Duncan, B.N., Streets, D.G., Eskes, H., A, R. van der, McLinden, C., Fioletov, V., Carn, S., Laat, J. de, DeLand, M., Marchenko, S., McPeters, R., Ziemke, J., Fu, D., Liu, X., Pickering, K., Apituley, A., González Abad, G., Arola, A., Boersma, F., Chan Miller, C., Chance, K., Graaf, M. de, Hakkarainen, J., Hassinen, S., Ialongo, I., Kleipool, Q., Krotkov, N., Li, C., Lamsal, L., Newman, P., Nowlan, C., Suleiman, R., Tilstra, L.G., Torres, O., Wang, H., Wargan, K., 2018. The Ozone Monitoring Instrument: overview of 14 years in space. Atmospheric Chemistry and Physics 18, 5699–5745. https://doi.org/10.5194/acp-18-5699-2018

Li, C., Martin, R.V., Shephard, M.W., Cady-Pereira, K., Cooper, M.J., Kaiser, J., Lee, C.J., Zhang, L., Henze, D.K., 2019. Assessing the Iterative Finite Difference Mass Balance and 4D-Var Methods to Derive Ammonia Emissions Over North America Using Synthetic Observations. Journal of Geophysical Research: Atmospheres 124, 4222–4236. https://doi.org/10.1029/2018JD030183

Li, K., Jacob, D.J., Liao, H., Shen, L., Zhang, Q., Bates, K.H., 2019. Anthropogenic drivers of 2013–2017 trends in summer surface ozone in China. PNAS 116, 422–427. https://doi.org/10.1073/pnas.1812168116

Li, M., Zhang, Q., Kurokawa, J., Woo, J.-H., He, K., Lu, Z., Ohara, T., Song, Y., Streets, D.G., Carmichael, G.R., Cheng, Y., Hong, C., Huo, H., Jiang, X., Kang, S., Liu, F., Su, H., Zheng, B., 2017a. MIX: a mosaic Asian anthropogenic emission inventory under the international collaboration framework of the MICS-Asia and HTAP. Atmospheric Chemistry and Physics 17, 935–963. https://doi.org/10.5194/acp-17-935-2017

Li, M., Zhang, Q., Zheng, B., Tong, D., Lei, Y., Liu, F., Hong, C., Kang, S., Yan, L., Zhang, Y., Bo, Y., Su, H., Cheng, Y., He, K., 2019. Persistent growth of anthropogenic non-methane volatile organic compound (NMVOC) emissions in China during 1990–2017: drivers, speciation and ozone formation potential. Atmospheric Chemistry and Physics 19, 8897–8913. https://doi.org/10.5194/acp-19-8897-2019

Lin, M., Horowitz, L.W., Payton, R., Fiore, A.M., Tonnesen, G., 2017. US surface ozone trends and extremes from 1980 to 2014: quantifying the roles of rising Asian emissions, domestic controls, wildfires, and climate. Atmospheric Chemistry and Physics 17, 2943–2970. https://doi.org/10.5194/acp-17-2943-2017

Liu, F., Zhang, Q., A, R.J. van der, Zheng, B., Tong, D., Yan, L., Zheng, Y., He, K., 2016. Recent reduction in NO x emissions over China: synthesis of satellite observations and emission inventories. Environ. Res. Lett. 11, 114002. https://doi.org/10.1088/1748-9326/11/11/114002

Liu, X., Mizzi, A.P., Anderson, J.L., Fung, I.Y., Cohen, R.C., 2017. Assimilation of satellite NO2 observations at high spatial resolution using OSSEs. Atmospheric Chemistry and Physics 17, 7067–7081. https://doi.org/10.5194/acp-17-7067-2017

Liu, Y., Shao, M., Fu, L., Lu, S., Zeng, L., Tang, D., 2008a. Source profiles of volatile organic compounds (VOCs) measured in China: Part I. Atmospheric Environment, PRIDE-PRD

2004 Campaign : Program of Regional Integrated Experiments on Air Quality over Pearl River Delta of China 42, 6247–6260. https://doi.org/10.1016/j.atmosenv.2008.01.070

Liu, Y., Shao, M., Lu, S., Chang, C.-C., Wang, J.-L., Fu, L., 2008b. Source apportionment of
740   ambient volatile organic compounds in the Pearl River Delta, China: Part II. Atmospheric Environment, PRIDE-PRD 2004 Campaign : Program of Regional Integrated Experiments on Air Quality over Pearl River Delta of China 42, 6261–6274. https://doi.org/10.1016/j.atmosenv.2008.02.027

Lu, X., Zhang, L., Chen, Y., Zhou, M., Zheng, B., Li, K., Liu, Y., Lin, J., Fu, T.-M., Zhang, Q.,
745   2019. Exploring 2016–2017 surface ozone pollution over China: source contributions and meteorological influences. Atmospheric Chemistry and Physics 19, 8339–8361. https://doi.org/10.5194/acp-19-8339-2019

Logan, J.A., 1983. Nitrogen oxides in the troposphere: Global and regional budgets. Journal of Geophysical Research: Oceans 88, 10785–10807.
750   https://doi.org/10.1029/JC088iC15p10785

Marais, E.A., Jacob, D.J., Kurosu, T.P., Chance, K., Murphy, J.G., Reeves, C., Mills, G., Casadio, S., Millet, D.B., Barkley, M.P., Paulot, F., Mao, J., 2012b. Isoprene emissions in Africa inferred from OMI observations of formaldehyde columns. Atmospheric Chemistry and Physics 12, 6219–6235. https://doi.org/10.5194/acp-12-6219-2012

755   Martin, R.V., Jacob, D.J., Chance, K., Kurosu, T.P., Palmer, P.I., Evans, M.J., 2003. Global inventory of nitrogen oxide emissions constrained by space-based observations of NO2 columns. Journal of Geophysical Research: Atmospheres 108. https://doi.org/10.1029/2003JD003453

Millet, D.B., Jacob, D.J., Boersma, K.F., Fu, T.-M., Kurosu, T.P., Chance, K., Heald, C.L.,
760   Guenther, A., 2008b. Spatial distribution of isoprene emissions from North America derived from formaldehyde column measurements by the OMI satellite sensor. Journal of Geophysical Research: Atmospheres 113. https://doi.org/10.1029/2007JD008950

Miyazaki, K., Eskes, H., Sudo, K., Boersma, K.F., Bowman, K., Kanaya, Y., 2017. Decadal changes in global surface NOx emissions from multi-constituent satellite data
765   assimilation. Atmospheric Chemistry and Physics 17, 807–837. https://doi.org/10.5194/acp-17-807-2017

Miyazaki, K., Sekiya, T., Fu, D., Bowman, K.W., Kulawik, S.S., Sudo, K., Walker, T., Kanaya, Y., Takigawa, M., Ogochi, K., Eskes, H., Boersma, K.F., Thompson, A.M., Gaubert, B., Barre, J., Emmons, L.K., 2019. Balance of Emission and Dynamical Controls on Ozone
770   During the Korea-United States Air Quality Campaign From Multiconstituent Satellite Data Assimilation. Journal of Geophysical Research: Atmospheres 124, 387–413. https://doi.org/10.1029/2018JD028912

Palmer, P.I., Jacob, D.J., Fiore, A.M., Martin, R.V., Chance, K., Kurosu, T.P., 2003. Mapping isoprene emissions over North America using formaldehyde column observations from
775   space. Journal of Geophysical Research: Atmospheres 108. https://doi.org/10.1029/2002JD002153

Paulson, S.E., Orlando, J.J., 1996. The reactions of ozone with alkenes: An important source of HOx in the boundary layer. Geophysical Research Letters 23, 3727–3730. https://doi.org/10.1029/96GL03477

780   Reuter, M., Buchwitz, M., Hilboll, A., Richter, A., Schneising, O., Hilker, M., Heymann, J., Bovensmann, H., Burrows, J.P., 2014. Decreasing emissions of NO x relative to CO 2 in

East Asia inferred from satellite observations. Nature Geoscience 7, 792–795. https://doi.org/10.1038/ngeo2257

Rodgers, C.D., 2000. Inverse Methods for Atmospheric Sounding: Theory and Practice. WORLD SCIENTIFIC. https://doi.org/10.1142/3171

Romer Present, P.S., Zare, A., Cohen, R.C., 2020. The changing role of organic nitrates in the removal and transport of NOx. Atmospheric Chemistry and Physics 20, 267–279. https://doi.org/10.5194/acp-20-267-2020

Schroeder, J.R., Crawford, J.H., Fried, A., Walega, J., Weinheimer, A., Wisthaler, A., Müller, M., Mikoviny, T., Chen, G., Shook, M., Blake, D.R., Tonnesen, G.S., 2017. New insights into the column CH2O/NO2 ratio as an indicator of near-surface ozone sensitivity. Journal of Geophysical Research: Atmospheres 122, 8885–8907. https://doi.org/10.1002/2017JD026781

Shen, L., Jacob, D.J., Zhu, L., Zhang, Q., Zheng, B., Sulprizio, M.P., Li, K., Smedt, I.D., Abad, G.G., Cao, H., Fu, T.-M., Liao, H., 2019. The 2005–2016 Trends of Formaldehyde Columns Over China Observed by Satellites: Increasing Anthropogenic Emissions of Volatile Organic Compounds and Decreasing Agricultural Fire Emissions. Geophysical Research Letters 46, 4468–4475. https://doi.org/10.1029/2019GL082172

Shim, C., Wang, Y., Choi, Y., Palmer, P.I., Abbot, D.S., Chance, K., 2005. Constraining global isoprene emissions with Global Ozone Monitoring Experiment (GOME) formaldehyde column measurements. Journal of Geophysical Research: Atmospheres 110. https://doi.org/10.1029/2004JD005629

Skamarock, W.C., Klemp, J.B., 2008. A time-split nonhydrostatic atmospheric model for weather research and forecasting applications. Journal of Computational Physics, Predicting weather, climate and extreme events 227, 3465–3485. https://doi.org/10.1016/j.jcp.2007.01.037

Souri, A.H., Choi, Y., Jeon, W., Li, X., Pan, S., Diao, L., Westenbarger, D.A., 2016a. Constraining NOx emissions using satellite NO2 measurements during 2013 DISCOVER-AQ Texas campaign. Atmospheric Environment 131, 371–381. https://doi.org/10.1016/j.atmosenv.2016.02.020

Souri, A.H., Choi, Y., Li, X., Kotsakis, A., Jiang, X., 2016b. A 15-year climatology of wind pattern impacts on surface ozone in Houston, Texas. Atmospheric Research 174–175, 124–134. https://doi.org/10.1016/j.atmosres.2016.02.007

Souri, A.H., Choi, Y., Jeon, W., Woo, J.-H., Zhang, Q., Kurokawa, J., 2017a. Remote sensing evidence of decadal changes in major tropospheric ozone precursors over East Asia. Journal of Geophysical Research: Atmospheres 122, 2474–2492. https://doi.org/10.1002/2016JD025663

Souri, A.H., Choi, Y., Jeon, W., Kochanski, A.K., Diao, L., Mandel, J., Bhave, P.V., Pan, S., 2017b. Quantifying the Impact of Biomass Burning Emissions on Major Inorganic Aerosols and Their Precursors in the U.S. Journal of Geophysical Research: Atmospheres 122, 12,020-12,041. https://doi.org/10.1002/2017JD026788

Souri, A.H., Choi, Y., Pan, S., Curci, G., Nowlan, C.R., Janz, S.J., Kowalewski, M.G., Liu, J., Herman, J.R., Weinheimer, A.J., 2018. First Top-Down Estimates of Anthropogenic NOx Emissions Using High-Resolution Airborne Remote Sensing Observations. Journal of Geophysical Research: Atmospheres 123, 3269–3284. https://doi.org/10.1002/2017JD028009

Souri, A.H., Nowlan, C.R., Wolfe, G.M., Lamsal, L.N., Chan Miller, C.E., Abad, G.G., Janz, S.J., Fried, A., Blake, D.R., Weinheimer, A.J., Diskin, G.S., Liu, X., Chance, K., 2020. Revisiting the effectiveness of HCHO/NO2 ratios for inferring ozone sensitivity to its precursors using high resolution airborne remote sensing observations in a high ozone episode during the KORUS-AQ campaign. Atmospheric Environment 117341. https://doi.org/10.1016/j.atmosenv.2020.117341

Spurr, R.J.D., 2006. VLIDORT: A linearized pseudo-spherical vector discrete ordinate radiative transfer code for forward model and retrieval studies in multilayer multiple scattering media. Journal of Quantitative Spectroscopy and Radiative Transfer 102, 316–342. https://doi.org/10.1016/j.jqsrt.2006.05.005

Stavrakou, T., Guenther, A., Razavi, A., Clarisse, L., Clerbaux, C., Coheur, P.-F., Hurtmans, D., Karagulian, F., Mazière, M.D., Vigouroux, C., Amelynck, C., Schoon, N., Laffineur, Q., Heinesch, B., Aubinet, M., Rinsland, C., Müller, J.-F., 2011. First space-based derivation of the global atmospheric methanol emission fluxes. Atmospheric Chemistry and Physics 11, 4873–4898. https://doi.org/10.5194/acp-11-4873-2011

Stavrakou, T., Müller, J.-F., Bauwens, M., De Smedt, I., 2017. Sources and Long-Term Trends of Ozone Precursors to Asian Pollution, in: Bouarar, I., Wang, X., Brasseur, G.P. (Eds.), Air Pollution in Eastern Asia: An Integrated Perspective, ISSI Scientific Report Series. Springer International Publishing, Cham, pp. 167–189. https://doi.org/10.1007/978-3-319-59489-7_8

Stavrakou, T., Müller, J.-F., Smedt, I.D., Roozendael, M.V., Werf, G.R. van der, Giglio, L., Guenther, A., 2009. Global emissions of non-methane hydrocarbons deduced from SCIAMACHY formaldehyde columns through 2003–2006. Atmospheric Chemistry and Physics 9, 3663–3679. https://doi.org/10.5194/acp-9-3663-2009

Trappey, A.J.C., Trappey, C., Hsiao, C.T., Ou, J.J.R., Li, S.J., Chen, K.W.P., 2012. An evaluation model for low carbon island policy: The case of Taiwan's green transportation policy. Energy Policy 45, 510–515. https://doi.org/10.1016/j.enpol.2012.02.063

Travis, K.R., Jacob, D.J., Fisher, J.A., Kim, P.S., Marais, E.A., Zhu, L., Yu, K., Miller, C.C., Yantosca, R.M., Sulprizio, M.P., Thompson, A.M., Wennberg, P.O., Crounse, J.D., Clair, J.M.S., Cohen, R.C., Laughner, J.L., Dibb, J.E., Hall, S.R., Ullmann, K., Wolfe, G.M., Pollack, I.B., Peischl, J., Neuman, J.A., Zhou, X., 2016. Why do models overestimate surface ozone in the Southeast United States? Atmospheric Chemistry and Physics 16, 13561–13577. https://doi.org/10.5194/acp-16-13561-2016

Turner, A.J., Jacob, D.J., 2015. Balancing aggregation and smoothing errors in inverse models. Atmospheric Chemistry and Physics 15, 7039–7048. https://doi.org/10.5194/acp-15-7039-2015

Valin, L.C., Fiore, A.M., Chance, K., Abad, G.G., 2016. The role of OH production in interpreting the variability of CH2O columns in the southeast U.S. Journal of Geophysical Research: Atmospheres 121, 478–493. https://doi.org/10.1002/2015JD024012

Wells, K.C., Millet, D.B., Cady-Pereira, K.E., Shephard, M.W., Henze, D.K., Bousserez, N., Apel, E.C., de Gouw, J., Warneke, C., Singh, H.B., 2014. Quantifying global terrestrial methanol emissions using observations from the TES satellite sensor. Atmospheric Chemistry and Physics 14, 2555–2570. https://doi.org/10.5194/acp-14-2555-2014

Wiedinmyer, C., Akagi, S.K., Yokelson, R.J., Emmons, L.K., Al-Saadi, J.A., Orlando, J.J., Soja, A.J., 2011. The Fire INventory from NCAR (FINN): a high resolution global model to

estimate the emissions from open burning. Geoscientific Model Development 4, 625–641. https://doi.org/10.5194/gmd-4-625-2011

875   Wolfe, G.M., Kaiser, J., Hanisco, T.F., Keutsch, F.N., Gouw, J.A. de, Gilman, J.B., Graus, M., Hatch, C.D., Holloway, J., Horowitz, L.W., Lee, B.H., Lerner, B.M., Lopez-Hilifiker, F., Mao, J., Marvin, M.R., Peischl, J., Pollack, I.B., Roberts, J.M., Ryerson, T.B., Thornton, J.A., Veres, P.R., Warneke, C., 2016. Formaldehyde production from isoprene oxidation across NOx regimes. Atmospheric Chemistry and Physics 16, 2597–2610.
880   https://doi.org/10.5194/acp-16-2597-2016

Zhang, Q., He, K., Huo, H., 2012. Cleaning China's air. Nature 484, 161–162. https://doi.org/10.1038/484161a

Zhong, L., Louie, P.K.K., Zheng, J., Yuan, Z., Yue, D., Ho, J.W.K., Lau, A.K.H., 2013. Science–policy interplay: Air quality management in the Pearl River Delta region and
885   Hong Kong. Atmospheric Environment, Improving Regional Air Quality over the Pearl River Delta and Hong Kong: from Science to Policy 76, 3–10. https://doi.org/10.1016/j.atmosenv.2013.03.012

Zhu, L., González Abad, G., Nowlan, C.R., Chan Miller, C., Chance, K., Apel, E.C., DiGangi, J.P., Fried, A., Hanisco, T.F., Hornbrook, R.S., Hu, L., Kaiser, J., Keutsch, F.N., Permar,
890   W., Clair, J.M.S., Wolfe, G.M., 2020. Validation of satellite formaldehyde (HCHO) retrievals using observations from 12 aircraft campaigns. Atmospheric Chemistry and Physics Discussions 1–25. https://doi.org/10.5194/acp-2019-1117

Zhu, L., Jacob, D.J., Kim, P.S., Fisher, J.A., Yu, K., Travis, K.R., Mickley, L.J., Yantosca, R.M., Sulprizio, M.P., Smedt, I.D., González Abad, G., Chance, K., Li, C., Ferrare, R., Fried,
895   A., Hair, J.W., Hanisco, T.F., Richter, D., Jo Scarino, A., Walega, J., Weibring, P., Wolfe, G.M., 2016. Observing atmospheric formaldehyde (HCHO) from space: validation and intercomparison of six retrievals from four satellites (OMI, GOME2A, GOME2B, OMPS) with SEAC4RS aircraft observations over the southeast US. Atmospheric Chemistry and Physics 16, 13477–13490. https://doi.org/10.5194/acp-16-
900   13477-2016

Table 1. CMAQ major configurations

CMAQ version	V5.2.1
Chemical Mechanism	CB05 with chlorine chemistry
Lightning NO_x emission	Included using inline code
Photolysis	Inline including aerosol impacts
Horizontal advection	YAMO (hyamo)
Vertical advection	WRF omega formula (vwrf)
Horizontal mixing/diffusion	Multiscale (multiscale)
Vertical mixing/diffusion	Asymmetric Convective Model version 2 (acm2)
Aerosol	AERO 6 for sea salt and thermodynamics (aero6)
IC/BC source	GEOS-Chem v10

Table 2. WRF physics options

WRF Version	V3.9.1
Microphysics	WSM-6
Long-wave Radiation	RRTMG
Short-wave Radiation	RRTMG
Surface Layer Option	Monin-Obukhov
Land-Surface Option	Noah LSM
Boundary Layer	ACM2
Cumulus Cloud Option	Kain-Fritsch
IC/BC	FNL 0.25º

905

Table 3. The uncertainty assumptions used for estimating the covariance matrix of the a priori.

	Anthropogenic	Biogenic	Biomass Burning
NO_x	50%	200%	100%
VOC	150%	200%	300%

Table 4. Statistics of surface temperature, relative humidity, and wind. Corr – Correlation;; RMSE – Root Mean Square Error; MAE – Mean Absolute Error; MB – Mean Bias; O – Observation; M - Model; O_M – Observed Mean; M_M – Model Mean; SD – Standard Deviation; Units for RMSE/MAE/MB/O_M/M_M/O_SD/M_SD: ºC for temperature, percentage for relative humidity, and m s^{-1} for wind.

910

Variable	Corr	RMSE	MAE	MB	O_M	M_M	O_SD	M_SD
Temperature	0.74	7.0	2.8	0.6	22.2	22.8	9.5	8.7
Relative Humidity	0.76	12.1	9.5	-1.1	67.8	66.6	14.3	18.6
U Wind	0.58	1.3	0.7	0.1	0.1	0.2	1.2	1.4
V Wind	0.49	1.6	0.7	0.3	0.2	0.5	1.6	1.2

Table 5. NO_x emissions before and after carrying out the inversion using OMI/OMPS for different countries in May-June 2016.

Countries	The a priori (Gg/day)	The a posteriori (Gg/day)	Changes in magnitudes	Changes in errors
China	87.94±44.09[1]	68.00±15.94[2]	-23%	-63%
North China Plain	27.96±13.49	19.05±2.50	-32%	-81%
Pearl River Delta	4.23±1.78	2.70±0.32	-36%	-84%
Yangtze River Delta	9.84±4.68	5.77±0.51	-41%	-89%
Thailand	4.38±3.24	4.20±2.28	-4%	-29%
Japan	3.53±1.71	3.96±1.04	+12%	-39%
Malaysia	2.89±2.77	2.25±1.34	-22%	-49%
Vietnam	2.87±2.04	2.79±1.57	-3%	-23%
South Korea	2.71±1.34	2.95±0.58	+9%	-56%
Bangladesh	1.72±1.06	2.10±0.87	+22%	-18%
Philippines	1.30±1.10	1.54±0.98	+18%	-11%
Taiwan	1.26±0.57	0.97±0.33	-23%	-42%
Cambodia	0.54±0.50	0.57±0.45	+5%	-11%
Mongolia	0.19±0.13	0.28±0.12	+44%	-8%

1- The errors in the a priori are estimated from equation 6.
2- The errors in the a posteriori are calculated by equation 4.

920   **Table 6.** MDA8 surface ozone levels before and after carrying out the inversion for different regions in May-June 2016.

Regions	The a priori (ppbv)	The a posteriori (ppbv)	Changes in magnitudes
China	56.10±16.34	56.72±16.71	+1.1%
North China Plain	81.15±9.57	85.71±10.39	+5.6%
Pearl River Delta	65.94±9.39	62.37±8.93	-5.4%
Yangtze River Delta	76.79±5.90	82.04±5.21	+6.8%
Thailand	50.86±8.84	48.85±7.94	-3.9%
Japan	64.29±7.98	65.52±7.78	+1.9%
Malaysia	46.87±21.87	44.22±12.90	-5.6%
Vietnam	49.90±9.20	48.88±8.65	-2.0%
South Korea	84.23±3.57	84.90±3.69	+0.8%
Bangladesh	65.79±12.08	65.21±12.20	-0.9%
Philippines	27.92±9.11	28.69±7.92	+2.8%
Taiwan	61.55±10.88	54.38±8.00	-11.6%
Cambodia	39.87±3.62	40.20±3.46	+0.8%
Mongolia	40.11±2.52	40.16±2.40	+0.1%

925

Figures:
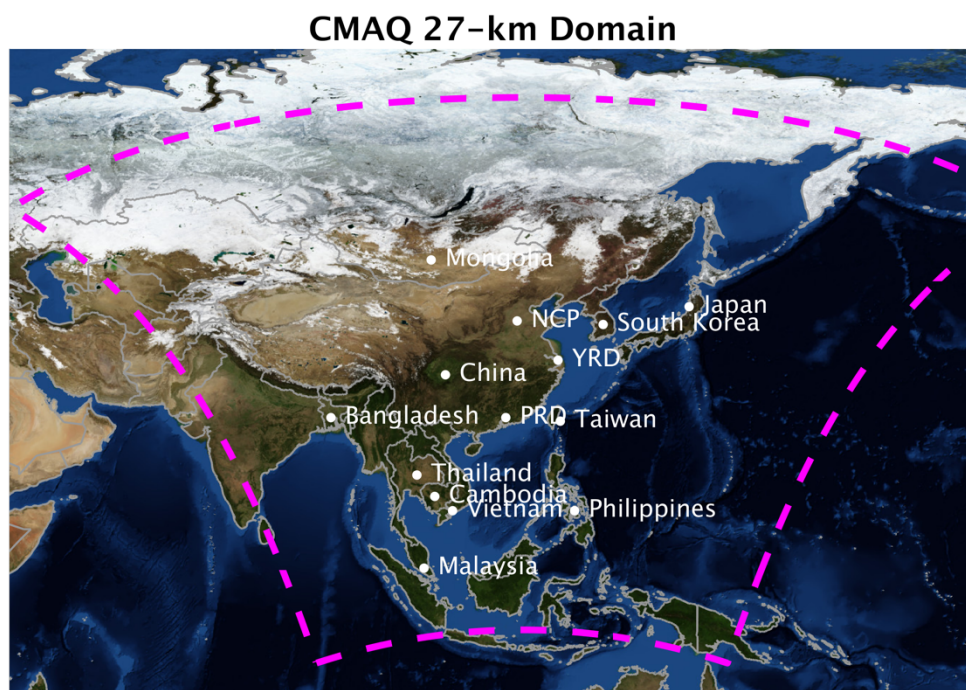
Figure 1. The CMAQ 27-km domain covering the major proportion of Asia. The background
picture is retrieved from publicly available NASA's blue marble (© NASA).
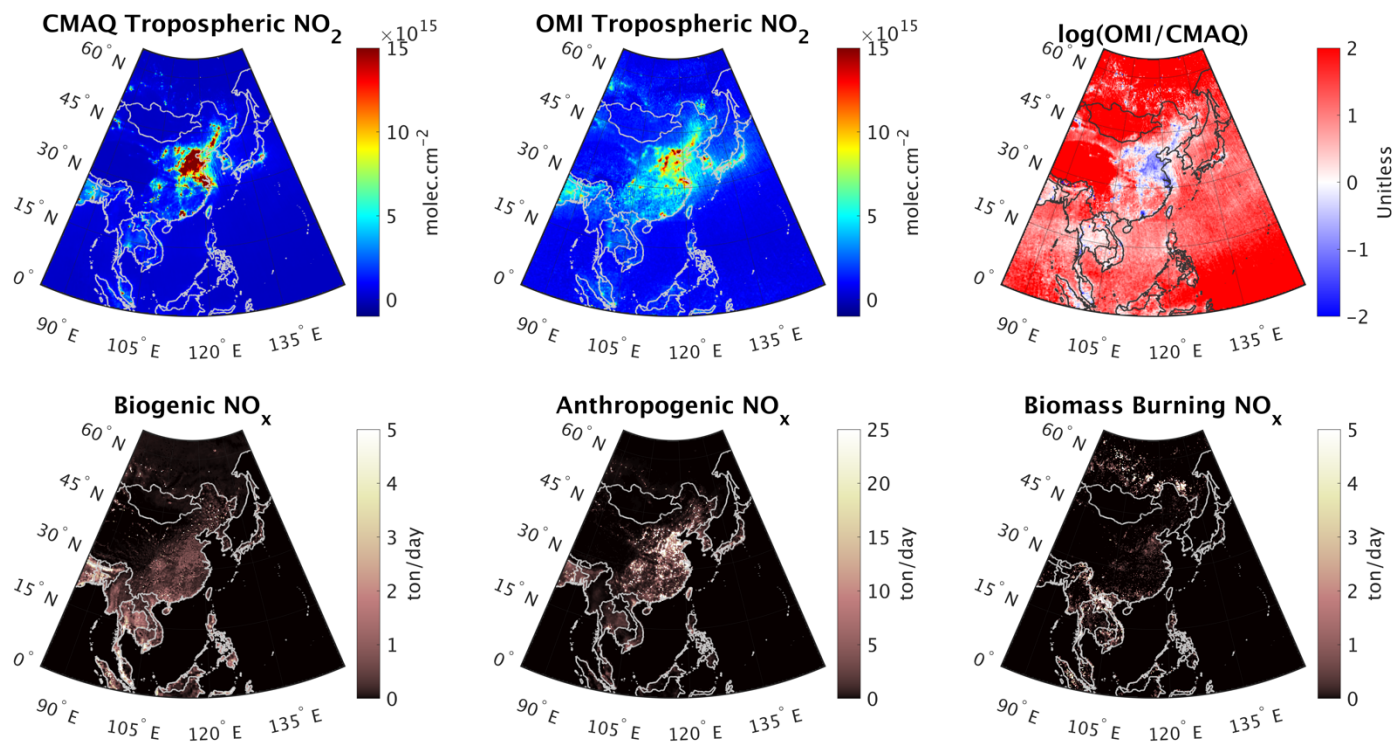
Figure 2. (first row), tropospheric NO_2 columns from the WRF-CMAQ model, OMI (using adjusted AMFs based on the shape factors derived from the model and bias corrected following Choi et al. [2019]), and the logarithmic ratio of CMAQ/OMI during May-June 2016 at ~1330 LST. (second row) The major sources of NO_x emissions in the region including biogenic (soil) emissions simulated by MEGAN, anthropogenic emissions estimated by MIX Asia (2010), and biomass burning emissions made by FINN. The emissions are the daily-mean values based on the emissions in May-June.
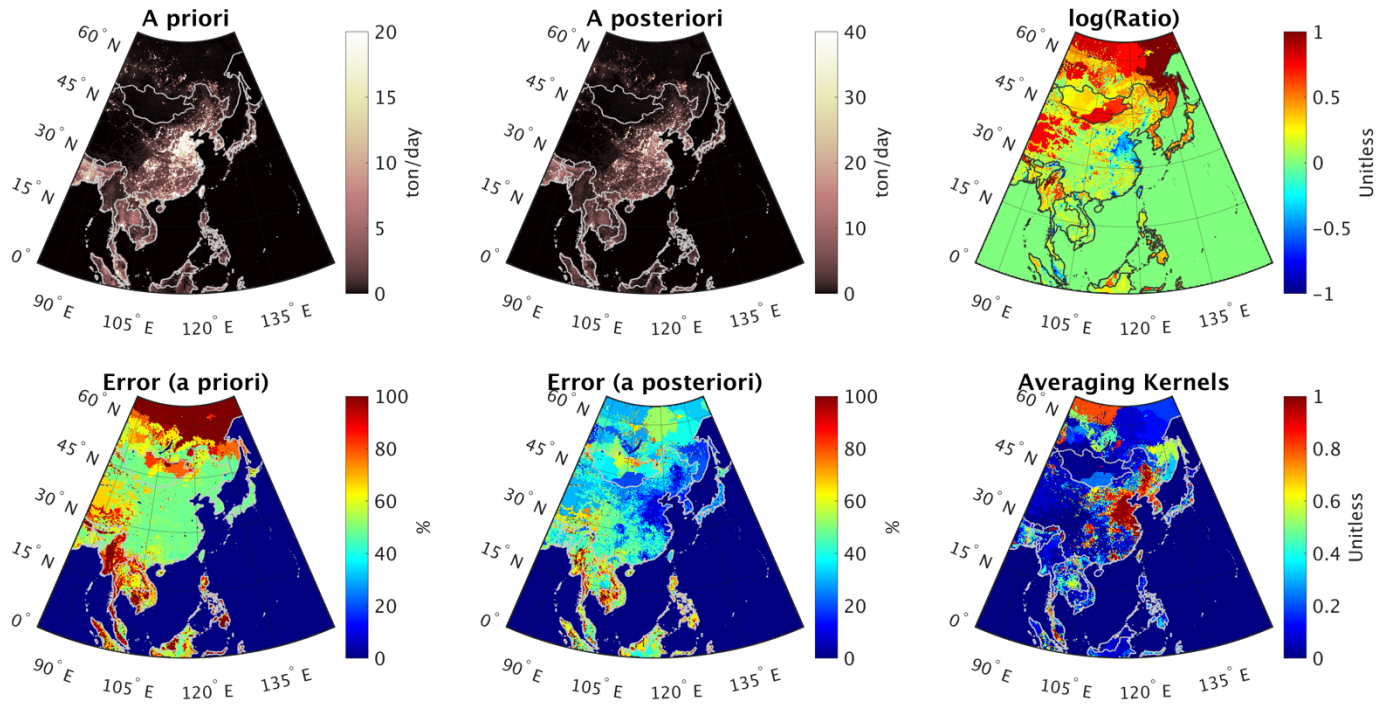
Figure 3. (first row), total NO$_x$ emissions (i.e., the a priori), constrained by the satellite observations (i.e., the a posteriori) in May-June 2016, and the ratio of the a posteriori to the a priori. (second row) the errors in the a priori based on Table 3, the errors in the top-down estimation, and the averaging kernels (AKs) obtained from the estimation.

945
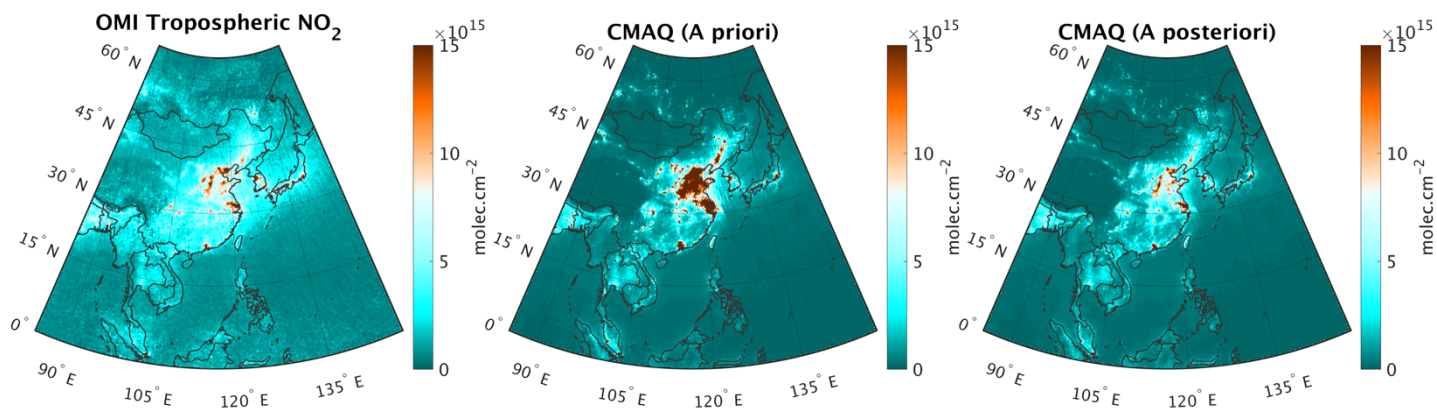
950 **Figure 4.** (from left to right), tropospheric NO_2 columns from OMI, WRF-CMAQ simulated with the prior emissions, and the same model but with the top-down emissions constrained by OMI/OMPS in May-June 2016.

955
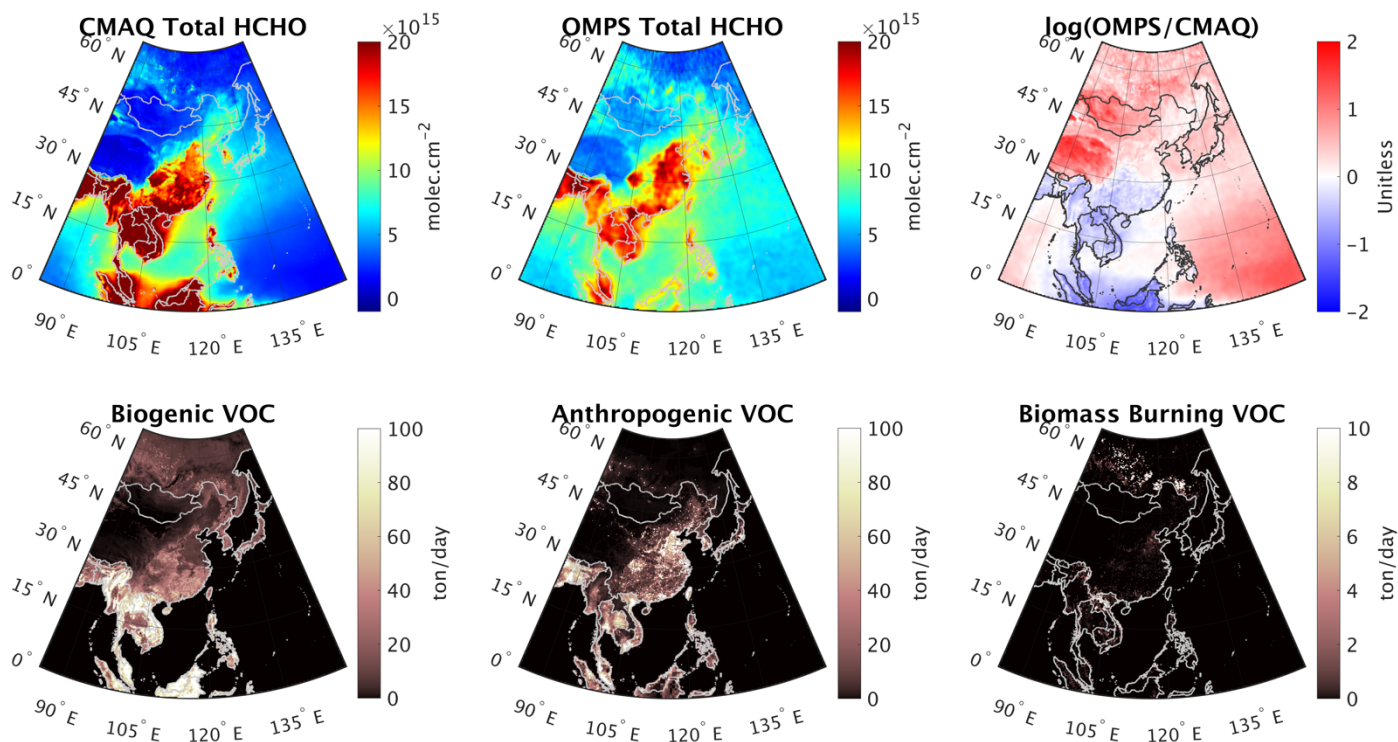
Figure 5. (first row), HCHO total columns from the WRF-CMAQ model, OMPS (using adjusted AMFs based on the shape factors derived from the model and bias corrected following the method proposed in Zhu et al. [2020]), and the logarithmic ratio of CMAQ/OMPS during May-June 2016 at ~1330 LST. (second row) The major sources of VOC emissions in the area including biogenic emissions simulated by MEGAN, anthropogenic emissions estimated by MIX Asia (2010), and biomass burning emissions made by FINN. The emissions are the daily-mean values based on the emissions in May-June. The VOC emissions only add up those compounds that are included in the CB05 mechanism.
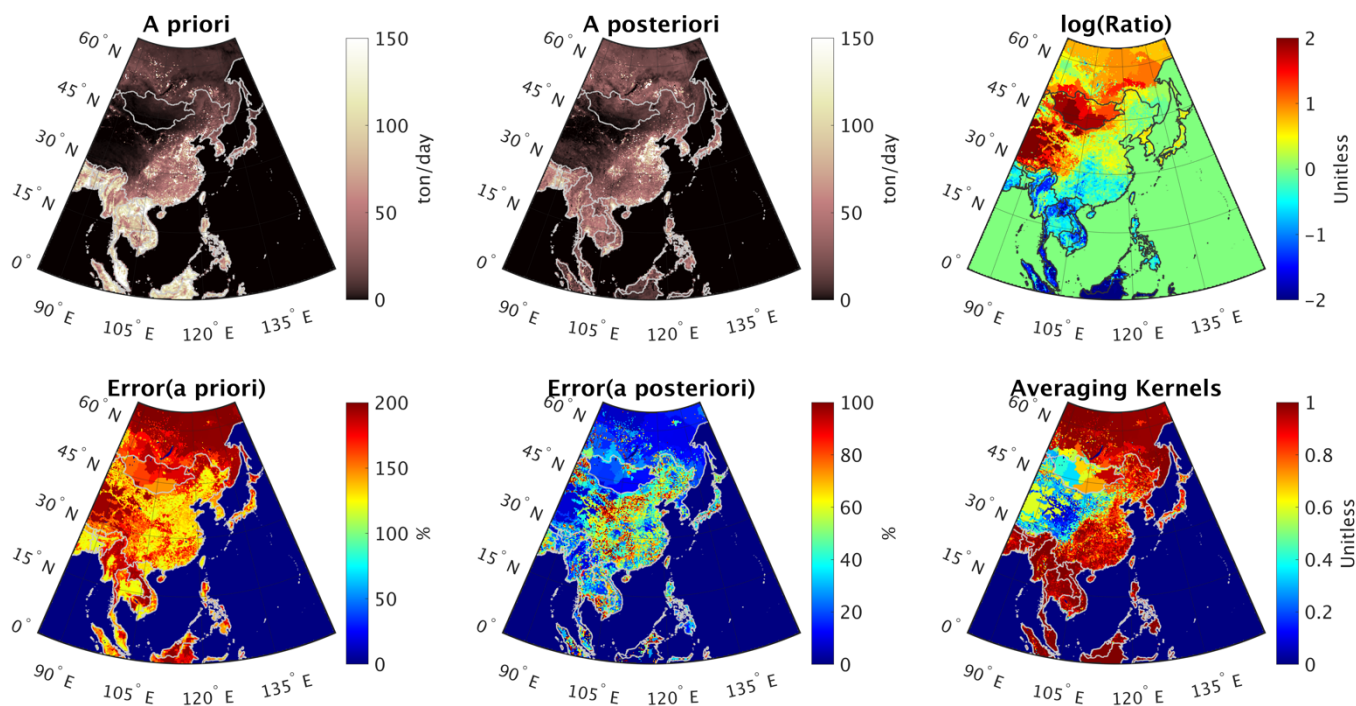
970 **Figure 6.** (first row), total VOC emissions (i.e., the a priori), constrained by the satellite observations (i.e., the a posteriori) in May-June 2016, and the ratio of the a posteriori to the a priori. (second row) the errors in the a priori based on Table 3, the errors in the top-down estimation, and the averaging kernels (AKs) obtained from the estimation.
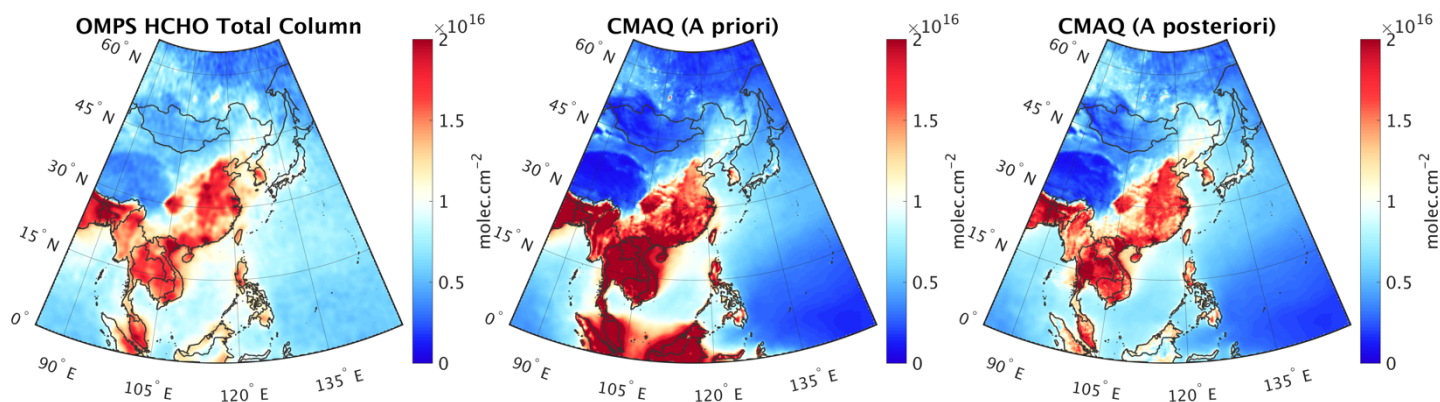
Figure 7. (from left to right), HCHO total columns from OMPS, the WRF-CMAQ simulated with the prior emissions, and the same model but with the top-down emissions constrained by the satellite in May-June 2016.
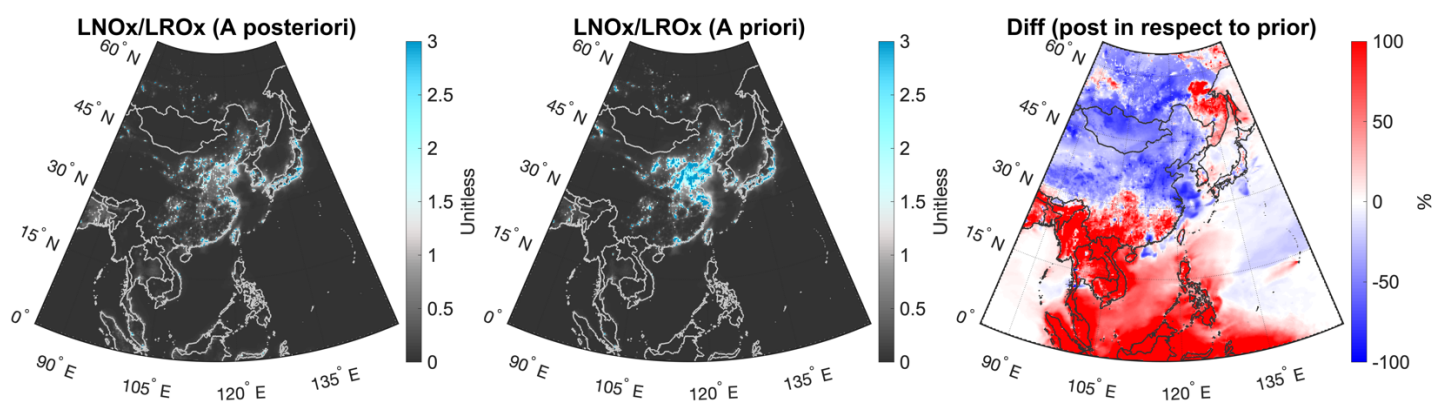
Figure 8. (from left to right), ratio of LNO_x/LRO_x simulated by the posterior emissions, the prior, and their relative differences at 1200-1800 CST, averaged over May-June 2016.
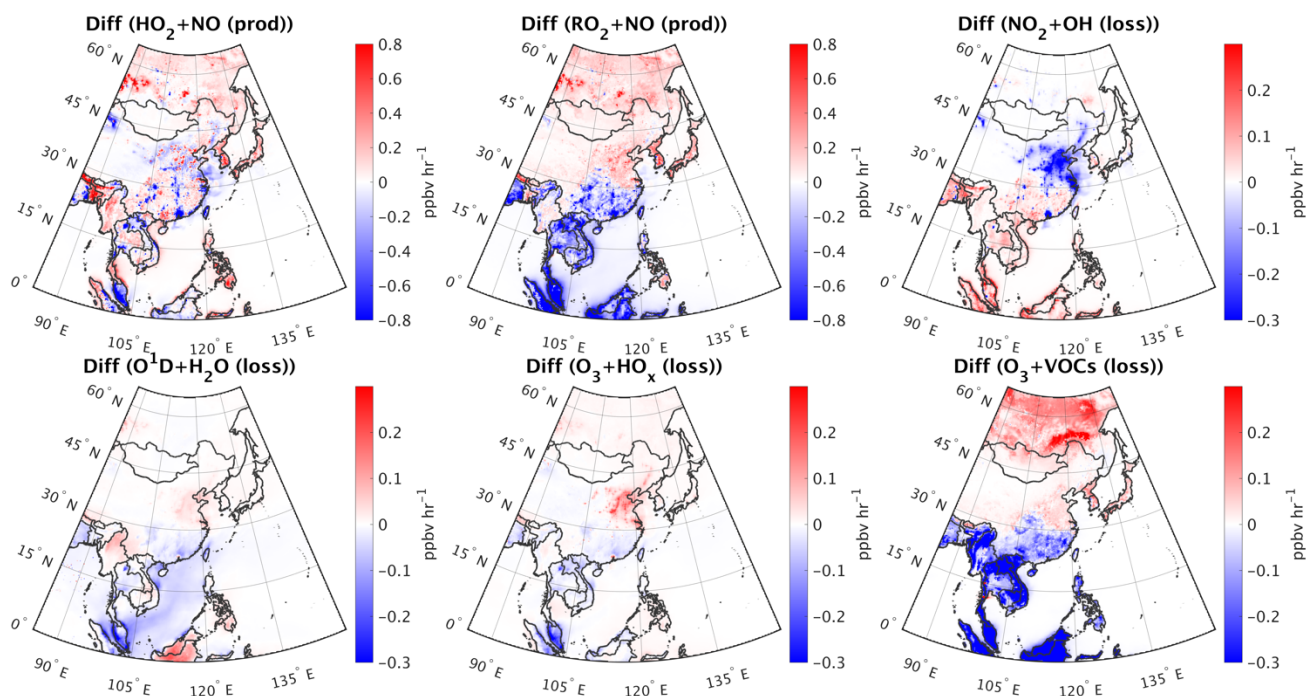
985 **Figure 9.** Differences between the simulations with the updated emissions and the default ones of six major pathways of ozone production/loss. The time period is May-June 2016, 1200-1800 CST.
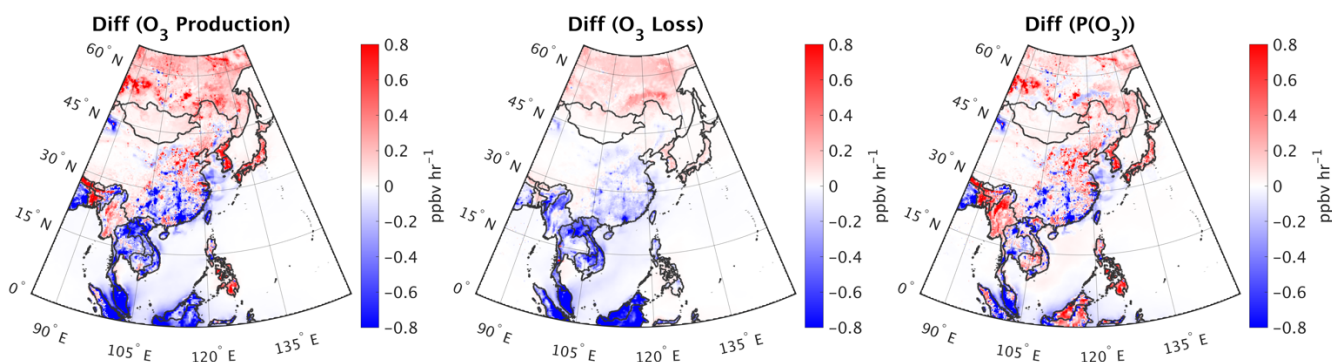
Figure 10. Changes in the major chemical pathways of ozone production/loss, and the net of ozone

990 production P(O₃) after updating the emissions. The time period is May-June 2016, 1200-1800 CST.
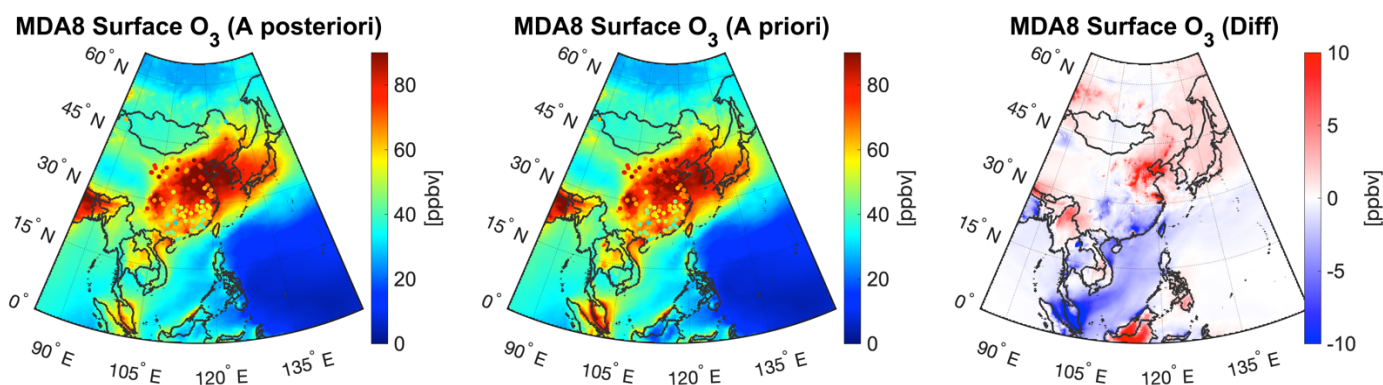
995 **Figure 11.** Simulated MDA8 surface ozone using the updated emissions constrained by OMI/OMPS observations (left), the default ones (middle), and their difference (right) in May-June 2016. We overplot surface MDA8 ozone values (circles) from the Chinese air quality monitoring network (https://quotsoft.net/air/).